Chapter 3

Algebraic Models

The simplest of all turbulence models are known as algebraic models. These models use the **Boussinesq eddy-viscosity approximation** to compute the Reynolds stress tensor as the product of an eddy viscosity and the mean strain-rate tensor. For computational simplicity, the eddy viscosity, in turn, is often computed in terms of a mixing length that is analogous to the mean free path in a gas. We will find that, in contrast to the molecular viscosity that is an intrinsic property of the fluid, the eddy viscosity (and hence the mixing length) depends upon the flow. Because the eddy viscosity and mixing length depend upon the particular flow under consideration they must be specified in advance. Thus, algebraic models are, by definition, **incomplete** models of turbulence.

We begin this chapter by first discussing molecular transport of momentum. Next we introduce Prandtl's mixing-length hypothesis and discuss its physical implications and limitations. The mixing-length model is then applied to free shear flows for which self-similar solutions hold. We discuss two modern algebraic turbulence models that are based on the mixing-length hypothesis, including applications to attached and separated wall-bounded flows. The latter applications illustrate the limit to the algebraic model's range of applicability. An interesting separated-flow replacement for algebraic models, known as the **Half-Equation Model**, improves agreement between computed and measured flow properties. The chapter concludes with a discussion of the range of applicability of algebraic models.

3.1 Molecular Transport of Momentum

To understand the motivation for the Boussinesq approximation, it is instructive to discuss momentum transport at the molecular level. However, as a word of caution, **molecules and turbulent eddies are fundamentally different**. They are so different that we will ultimately find, in Section 3.2, that the analogy between turbulent and molecular mixing is questionable, to say the least! It is nevertheless fruitful to pursue the analogy to illustrate how important it is to check the premises underlying turbulence closure approximations. At first glance, mimicking the molecular mixing process appears to be a careful exercise in physics. As we will see, the model just cannot stand up under close scrutiny.

We begin by considering a shear flow in which the velocity is given by

$$\mathbf{U} = U(y)\,\mathbf{i} \tag{3.1}$$

where $\mathbf{i}$ is a unit vector in the x direction. Figure 3.1 depicts such a flow. We consider the flux of momentum across the plane $y = 0$, noting that molecular motion is random in both magnitude and direction. Molecules migrating across $y = 0$ are **typical of where they come from**. That is, molecules moving up bring a momentum deficit and vice versa. This gives rise to a shear stress t_{xy}.

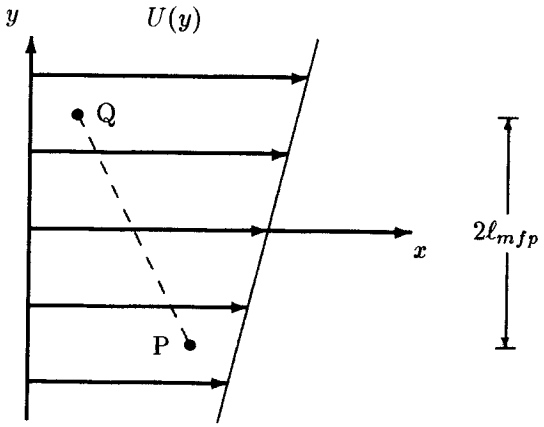

Figure 3.1: Shear flow schematic.

At the molecular level, we decompose the velocity according to

$$\mathbf{u} = \mathbf{U} + \mathbf{u}'' \tag{3.2}$$

where $\mathbf{U}$ is the average velocity defined in Equation (3.1) and $\mathbf{u}''$ represents the random molecular motion. The instantaneous flux of any property across $y = 0$ is proportional to the velocity normal to the plane which, for this flow, is simply v''. Thus, the instantaneous flux of x-directed momentum, dp_{xy}, across a differential surface area dS is

$$dp_{xy} = \rho(U + u'')v'' \, dS \tag{3.3}$$

Performing an ensemble average over all molecules, we find

$$dP_{xy} = \overline{\rho u'' v''} \, dS \tag{3.4}$$

By definition, the stress acting on $y = 0$ is given by $\sigma_{xy} = dP_{xy}/dS$. It is customary in fluid mechanics to set $\sigma_{ij} = p\delta_{ij} - t_{ij}$, where t_{ij} is the viscous stress tensor. Thus,

$$t_{xy} = -\overline{\rho u'' v''} \tag{3.5}$$

Equation (3.5) bears a strong resemblance to the Reynolds-stress tensor. This is not a coincidence. As pointed out by Tennekes and Lumley (1983), a stress that is generated as a momentum flux can always be written in this form. The only real difference is that, at the macroscopic level, the turbulent fluctuations, u' and v', appear in place of the random molecular fluctuations, u'' and v''. **This similarity is the basis of the Boussinesq eddy-viscosity approximation.**

Referring again to Figure 3.1, we can appeal to arguments from the kinetic theory of gases [e.g., Jeans (1962)] to determine t_{xy} in terms of $U(y)$ and the fluid viscosity, μ. First, consider the average number of molecules moving across unit area in the positive y direction. For a perfect gas, molecular velocities follow the Maxwellian distribution so that all directions are equally probable. The average molecular velocity is the thermal velocity, v_{th}, which is approximately 4/3 times the speed of sound in air. On average, half of the molecules move in the positive y direction while the other half move in the negative y direction. Also, the average vertical component of the velocity is $v_{th} \cos\phi$ where ϕ is the angle from the vertical. Integrating over a hemispherical shell, the average vertical speed is $v_{th}/2$. Thus, the average number of molecules moving across unit area in the positive y direction is $nv_{th}/4$, where n is the number of molecules per unit volume.

Now consider the transfer of momentum that occurs when molecules starting from point P cross the $y = 0$ plane. We assume molecules are **typical of where they come from** which, on the molecular scale, is one mean free path away, the mean free path being the average distance a molecule travels between collisions with other molecules. Each molecule starting from

a point P below $y = 0$ brings a momentum deficit of $m[U(0) - U(-\ell_{mfp})]$, where m is the molecular mass and ℓ_{mfp} is the mean free path. Hence, the momentum flux from below is

$$\Delta P_- = \frac{1}{4}\rho v_{th}[U(0) - U(-\ell_{mfp})] \approx \frac{1}{4}\rho v_{th}\ell_{mfp}\frac{dU}{dy} \tag{3.6}$$

We have replaced $U(-\ell_{mfp})$ by the first two terms of its Taylor-series expansion in Equation (3.6) and used the fact that $\rho = mn$. Similarly, molecules moving from a point Q above $y = 0$ bring a momentum surplus of $m[U(\ell_{mfp}) - U(0)]$, and the momentum flux from above is

$$\Delta P_+ = \frac{1}{4}\rho v_{th}[U(\ell_{mfp}) - U(0)] \approx \frac{1}{4}\rho v_{th}\ell_{mfp}\frac{dU}{dy} \tag{3.7}$$

Consequently, the net shearing stress is the sum of ΔP_- and ΔP_+, wherefore

$$t_{xy} = \Delta P_- + \Delta P_+ \approx \frac{1}{2}\rho v_{th}\ell_{mfp}\frac{dU}{dy} \tag{3.8}$$

Hence, we conclude that the shear stress resulting from molecular transport of momentum in a perfect gas is given by

$$t_{xy} = \mu\frac{dU}{dy} \tag{3.9}$$

where μ is the molecular viscosity defined by

$$\mu = \frac{1}{2}\rho v_{th}\ell_{mfp} \tag{3.10}$$

The arguments leading to Equations (3.9) and (3.10) are approximate and only roughly represent the true statistical nature of molecular motion. Interestingly, Jeans (1962) indicates that a precise analysis yields $\mu = 0.499 v_{th}\ell_{mfp}$, wherefore our approximate analysis is remarkably accurate! However, we have made two implicit assumptions in our analysis that require justification.

First, we have truncated the Taylor series appearing in Equations (3.6) and (3.7) at the linear terms. For this approximation to be valid, we must have $\ell_{mfp}|d^2U/dy^2| \ll |dU/dy|$. The length scale L defined by

$$L \equiv \frac{|dU/dy|}{|d^2U/dy^2|} \tag{3.11}$$

is a length scale characteristic of the mean flow. Thus, the linear relation between stress and strain-rate implied by Equation (3.9) is valid provided the Knudsen number, Kn, is very small, i.e.,

$$Kn = \ell_{mfp}/L \ll 1 \tag{3.12}$$

For most practical flow conditions, the mean free path is several orders of magnitude smaller than any characteristic length scale of the mean flow. Thus, Equation (3.12) is satisfied for virtually all engineering problems.

Second, in computing the rate at which molecules cross $y = 0$, we assumed that $\mathbf{u}''$ remained Maxwellian even in the presence of shear. This will be true if molecules experience many collisions on the time scale of the mean flow. Now, the average time between collisions is ℓ_{mfp}/v_{th}. The characteristic time scale for the mean flow is $|dU/dy|^{-1}$. Thus, we also require that

$$\ell_{mfp} \ll \frac{v_{th}}{|dU/dy|} \tag{3.13}$$

Since v_{th} is of the same order of magnitude as the speed of sound, the right-hand side of Equation (3.13) defines yet another mean-flow length scale. As above, the mean free path is several orders smaller than this length scale for virtually all flows of engineering interest.

3.2 The Mixing-Length Hypothesis

Prandtl (1925) put forth the mixing-length hypothesis. He visualized a simplified model for turbulent fluid motion in which fluid particles coalesce into lumps that cling together and move as a unit. He further visualized that in a shear flow such as that depicted in Figure 3.1, the lumps retain their x-directed momentum for a distance in the y direction, ℓ_{mix}, that he called the mixing length. In analogy to the molecular momentum transport process with Prandtl's lump of fluid replacing the molecule and ℓ_{mix} replacing ℓ_{mfp}, we can say that similar to Equation (3.8),

$$\tau_{xy} = \frac{1}{2}\rho v_{mix}\ell_{mix}\frac{dU}{dy} \tag{3.14}$$

The formulation is not yet complete because the **mixing velocity**, v_{mix}, has not been specified. Prandtl further postulated that

$$v_{mix} = \text{constant} \cdot \ell_{mix}\left|\frac{dU}{dy}\right| \tag{3.15}$$

which makes sense on dimensional grounds. Because ℓ_{mix} is not a physical property of the fluid, we can always absorb the constant in Equation (3.15)

and the factor 1/2 in Equation (3.14) in the mixing length. Thus, in analogy to Equations (3.9) and (3.10), Prandtl's mixing-length hypothesis leads to

$$\tau_{xy} = \mu_T \frac{dU}{dy} \tag{3.16}$$

where μ_T is the **eddy viscosity** given by

$$\mu_T = \rho \ell_{mix}^2 \left| \frac{dU}{dy} \right| \tag{3.17}$$

Our formulation still remains incomplete since we have replaced Boussinesq's empirical eddy viscosity, μ_T, with Prandtl's empirical mixing length, ℓ_{mix}. Prandtl postulated further that for flows near solid boundaries the mixing length is proportional to distance from the surface. This turns out to be a reasonably good approximation over a limited portion of a turbulent boundary layer. As we will see in Section 3.3, for free shear flows such as jets, wakes and mixing layers, the mixing length is proportional to the width of the layer, δ. However, each of these flows requires a different coefficient of proportionality between ℓ_{mix} and δ. The point is, the mixing length is different for each flow (its ratio to the flow width, for example) and must be known in advance to obtain a solution.

Note that Equation (3.17) can be deduced directly from dimensional analysis. Assuming molecular transport of momentum is unimportant relative to turbulent transport, we expect molecular viscosity has no significance in a dimensional analysis. The only other dimensional parameters available in a shear flow are the fluid density, ρ, our assumed mixing length, ℓ_{mix}, and the velocity gradient, dU/dy. (The eddy viscosity cannot depend upon U since that would violate Galilean invariance.) A straightforward dimensional analysis yields Equation (3.17).

Another interesting observation follows from replacing τ_{xy} by its definition so that

$$-\overline{u'v'} = \left| \ell_{mix} \frac{dU}{dy} \right|^2 \tag{3.18}$$

The mixing velocity, v_{mix}, must be proportional to an appropriate average of v' such as the RMS value defined by $v_{rms} = (\overline{v'^2})^{1/2}$. Also, Townsend (1976) states that in all turbulent shear flows, experimental measurements indicate

$$\left| -\overline{u'v'} \right| \approx 0.4 u_{rms} v_{rms} \tag{3.19}$$

Consequently, if $v_{rms} \sim v_{mix}$, comparison of Equations (3.15) and (3.18) shows that the mixing-length model implies v_{rms} and u_{rms} are of the same order of magnitude. This is generally true although u_{rms} is usually 25% to 75% larger than v_{rms}.

At this point, we need to examine the appropriateness of the mixing-length hypothesis in representing turbulent transport of momentum. Because we have made a direct analogy to the molecular transport process, we have implicitly made the same two basic assumptions we made for molecular transport. Specifically, we have assumed that the Boussinesq approximation holds and that the turbulence is unaltered by the mean shear. Unfortunately, neither condition is rigorously satisfied in practice!

Concerning the Boussinesq approximation, its applicability depends upon the Knudsen number being small. Close to a solid boundary, for example, the mixing length is approximately linear with distance from the surface, y. Specifically, measurements indicate that $\ell_{mix} \approx 0.41y$. In the same vicinity, the velocity follows the well-known law of the wall [see Schlichting (1979)], and the velocity gradient varies inversely with y. Thus, the length L defined in Equation (3.11) is equal to y. Consequently, the Knudsen number is of order one, i.e.,

$$Kn = \ell_{mix}/L \approx 0.41 \tag{3.20}$$

Hence, the linear stress/strain-rate relation of Equation (3.16) is suspect.

Concerning the effect of the mean shear on the turbulence, the assumed lifetime of Prandtl's lumps of fluid is ℓ_{mix}/v_{mix}. Reference to Equation (3.15) shows that this time is proportional to $|dU/dy|^{-1}$. Hence, the analog to Equation (3.13) is

$$\ell_{mix} \sim \frac{v_{mix}}{|dU/dy|} \tag{3.21}$$

Equation (3.21) tells us that the lumps of fluid will undergo changes as they travel from points P and Q toward $y = 0$. This is indeed consistent with the observed nature of turbulent shear flows. Tennekes and Lumley (1983) describe the situation by saying, "the general conclusion must be that turbulence in a shear flow cannot possibly be in a state of equilibrium which is independent of the flow field involved. The turbulence is continually trying to adjust to its environment, without ever succeeding."

Thus, the theoretical foundation of the mixing-length hypothesis is a bit flimsy to say the least. On the one hand, this is a forewarning that a turbulence model built on this foundation is unlikely to possess a very wide range of applicability. On the other hand, as the entire formulation is empirical in its essence, the usefulness of and justification for any of its approximations ultimately lies in how well the model performs in applications, and we defer to the applications of the following sections as its justification.

As a pleasant surprise, we will see that despite its theoretical shortcomings, the mixing-length model does an excellent job of reproducing experimental measurements. It can be easily calibrated for a specific class of flows,

and the model's predictions are consistent with measurements provided we don't depart too far from the established data base used to calibrate the mixing length. Eddy viscosity models based on the mixing length have been fine tuned for many flows since 1925, most notably by Cebeci and Smith (1974). Strictly speaking, the term **equilibrium** is nonsensical in the context of turbulent shear flows since, as noted above, turbulence is continually attempting to adjust to its environment, without ever succeeding. Nevertheless, most turbulence researchers describe certain flows as **equilibrium turbulent flows**. What they actually mean is a relatively simple flow with slowly varying properties. Most flows of this type can be accurately described by a mixing-length computation. In this spirit, a fitting definition of equilibrium turbulent flow might be a flow that can be accurately described using a mixing-length model!

3.3 Application to Free Shear Flows

Our first applications will be to incompressible **free shear flows**. A flow is termed free if it is not bounded by solid surfaces. Figure 3.2 illustrates three different types of free shear flows, viz., the **far wake**, the **mixing layer**, and the **jet**. A wake forms downstream of any object placed in a stream of fluid; we will consider only the two-dimensional wake. A mixing layer occurs between two parallel streams moving at different speeds; for the case shown in the figure, the lower stream is at rest. A jet occurs when fluid is ejected from a nozzle or orifice. We will assume the jet issues into a quiescent fluid, and we will analyze both the (two-dimensional) plane jet and the (axisymmetric) round jet.

All three of these flows approach what is known as **self similarity** far enough downstream that details of the geometry and flow conditions near $x = 0$ become unimportant. The velocity component $U(x, y)$, for example, can be expressed in the form

$$U(x, y) = u_o(x) F(y/\delta(x)) \tag{3.22}$$

This amounts to saying that two velocity profiles located at different x stations have the same shape when plotted in the scaled form $U(x, y)/u_o(x)$ versus $y/\delta(x)$. Flows with this property are also referred to as **self preserving**.

Free shear flows are interesting building-block cases to test a turbulence model on for several reasons. First, there are no solid boundaries so that we avoid the complications boundaries add to the complexity of a turbulent flow. Second, they are mathematically easy to calculate because similarity solutions exist, where the Reynolds-averaged equations of motion can be

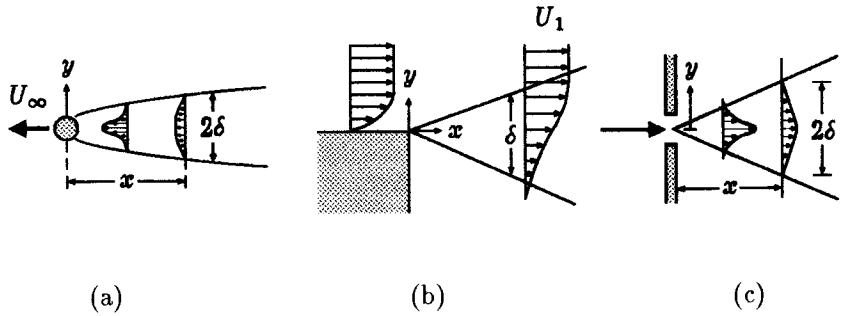

(a) (b) (c)

Figure 3.2: Free shear flows: (a) far wake; (b) mixing layer; and, (c) jet.

reduced to ordinary differential equations. This greatly simplifies the task of obtaining a solution. Third, there is a wealth of experimental data available to test model predictions against.

The standard boundary-layer approximations hold for all three of the shear flows considered in this Section. Additionally, molecular transport of momentum is negligible compared to turbulent transport. Since all three flows have constant pressure, the equations of motion are (with $j = 0$ for two-dimensional flow and $j = 1$ for axisymmetric flow):

$$\frac{\partial U}{\partial x} + \frac{1}{y^j}\frac{\partial}{\partial y}\left(y^j V\right) = 0 \tag{3.23}$$

$$\rho U\frac{\partial U}{\partial x} + \rho V\frac{\partial U}{\partial y} = \frac{1}{y^j}\frac{\partial}{\partial y}\left(y^j \tau_{xy}\right) \tag{3.24}$$

Of course, while the equations are the same for all three flows, boundary conditions are different. The appropriate boundary conditions will be stated when we discuss each flow.

As a historical note, in addition to the mixing-length model, Prandtl also proposed a simpler eddy viscosity model specifically for free shear flows. In this model,

$$\mu_T = \chi\rho[U_{max}(x) - U_{min}(x)]\delta(x) \tag{3.25}$$

where U_{max} and U_{min} are the maximum and minimum values of mean velocity in the layer, δ is the half width of the layer, and χ is a dimensionless empirical parameter. This model is very convenient for free shear flows because it is a function only of x by construction, and excellent results can be obtained if χ is assumed to be constant across the layer. Consequently, laminar flow solutions can be generalized for turbulent flow with,

at most, minor notation changes. We leave application of this model to the Problems section. All of the applications in this Section will be done using Equations (3.16) and (3.17).

We begin by analyzing the far wake in Subsection 3.3.1. Complete details of the similarity solution method are given for the benefit of the reader who has not had much experience with the method. The far wake is especially attractive as our first application because a simple closed-form solution can be obtained using the mixing-length model. Then, we proceed to the mixing layer in Subsection 3.3.2. While an analytical solution is possible for the mixing layer, numerical integration of the equations proves to be far simpler. Finally, we study the plane jet and the round jet in Subsection 3.3.3.

3.3.1 The Far Wake

Clearly the flow in the wake of the body indicated in Figure 3.2(a) is symmetric about the x axis. Thus, we solve for $0 \leq y < \infty$. The relevant boundary conditions follow from symmetry on the axis and the requirement that the velocity approach its freestream value far from the body. Hence, the boundary conditions are

$$U(x,y) \to U_\infty \quad \text{as} \quad y \to \infty \tag{3.26}$$

$$\frac{\partial U}{\partial y} = 0 \quad \text{at} \quad y = 0 \tag{3.27}$$

The classical approach to this problem is to linearize the momentum equation, an approximation that is strictly valid only in the far wake [Schlichting (1979)]. Thus, we say that

$$\mathbf{U}(x,y) = U_\infty \, \mathbf{i} - \hat{\mathbf{u}} \tag{3.28}$$

where $|\hat{\mathbf{u}}| \ll U_\infty$. The linearized momentum equation and boundary conditions become

$$\rho U_\infty \frac{\partial \hat{u}}{\partial x} = -\frac{\partial \tau_{xy}}{\partial y} \tag{3.29}$$

$$\hat{u}(x,y) \to 0 \quad \text{as} \quad y \to \infty \tag{3.30}$$

$$\frac{\partial \hat{u}}{\partial y} = 0 \quad \text{at} \quad y = 0 \tag{3.31}$$

There is also an integral constraint that must be satisfied by the solution. If we consider a control volume surrounding the body and extending to infinity, conservation of momentum leads to the following requirement [see Schlichting (1979)],

$$\int_0^\infty \rho U(U_\infty - U)\, dy = \frac{1}{2}D \tag{3.32}$$

where D is the drag of the body per unit width.

We use the mixing-length model to specify the Reynolds stress τ_{xy}, so that

$$\tau_{xy} = -\rho \ell_{mix}^2 \left|\frac{\partial \hat{u}}{\partial y}\right| \frac{\partial \hat{u}}{\partial y} \tag{3.33}$$

Finally, to close our set of equations, we assume the mixing length is proportional to the half-width of the wake, $\delta(x)$ [see Figure 3.2(a)]. Thus, we say that

$$\ell_{mix} = \alpha \delta(x) \tag{3.34}$$

where α is a constant that we refer to as a **closure coefficient**. Our fondest hope would be that the same value of α works for all free shear flows. Unfortunately, this is not the case so that the mixing-length model must be recalibrated for each type of shear flow.

To obtain the similarity solution to Equations (3.29) through (3.34), we proceed in a series of interrelated steps. The sequence is as follows.

1. Assume the form of the solution.
2. Transform the equations of motion.
3. Transform the boundary conditions and the integral constraint.
4. Determine the conditions required for existence of the similarity solution.
5. Solve the resulting ordinary differential equation subject to the transformed boundary conditions.

In addition to these 5 steps, we will also determine the value of the **closure coefficient** α in Equation (3.34) by comparison with experimental data.

Step 1. We begin by assuming the similarity solution can be written in terms of an as yet unknown velocity scale function, $u_o(x)$, and the wake half width, $\delta(x)$. Thus, we assume that the velocity can be written as

$$\hat{u}(x, y) = u_o(x) F(\eta) \tag{3.35}$$

where the **similarity variable**, η, is defined by

$$\eta = y/\delta(x) \tag{3.36}$$

Step 2. In order to transform Equation (3.29), we have to take account of the fact that we are making a formal change of dependent variables. We are transforming from (x, y) space to (x, η) space which means that derivatives must be transformed according to the chain rule of calculus. Thus, derivatives transform according to the following rules. Note that a subscript means that differentiation is done holding the subscripted variable constant.

$$\begin{aligned}\left(\frac{\partial}{\partial x}\right)_y &= \left(\frac{\partial x}{\partial x}\right)_y \left(\frac{\partial}{\partial x}\right)_\eta + \left(\frac{\partial \eta}{\partial x}\right)_y \left(\frac{\partial}{\partial \eta}\right)_x \\ &= \left(\frac{\partial}{\partial x}\right)_\eta + \left(\frac{\partial \eta}{\partial x}\right)_y \left(\frac{\partial}{\partial \eta}\right)_x \\ &= \left(\frac{\partial}{\partial x}\right)_\eta - \frac{\delta'(x)}{\delta(x)}\,\eta \left(\frac{\partial}{\partial \eta}\right)_x \end{aligned} \tag{3.37}$$

$$\begin{aligned}\left(\frac{\partial}{\partial y}\right)_x &= \left(\frac{\partial x}{\partial y}\right)_x \left(\frac{\partial}{\partial x}\right)_\eta + \left(\frac{\partial \eta}{\partial y}\right)_x \left(\frac{\partial}{\partial \eta}\right)_x \\ &= \left(\frac{\partial \eta}{\partial y}\right)_x \left(\frac{\partial}{\partial \eta}\right)_x \\ &= \frac{1}{\delta(x)} \left(\frac{\partial}{\partial \eta}\right)_x \end{aligned} \tag{3.38}$$

A prime denotes ordinary differentiation so that $\delta'(x) = d\delta/dx$ in Equation (3.37). We now proceed to transform Equation (3.29). For example, the derivatives of $\hat{u}$ are

$$\frac{\partial \hat{u}}{\partial x} = u_o' F(\eta) - \frac{u_o \delta'}{\delta} \eta \frac{dF}{d\eta} \tag{3.39}$$

$$\frac{\partial \hat{u}}{\partial y} = \frac{u_o}{\delta} \frac{dF}{d\eta} \tag{3.40}$$

Proceeding in this manner for all terms in Equation (3.29) and using the mixing-length prescription for the Reynolds stress leads to the transformed momentum equation.

$$\frac{U_\infty \delta u_o'}{u_o^2} F(\eta) - \frac{U_\infty \delta'}{u_o} \eta \frac{dF}{d\eta} = \alpha^2 \frac{d}{d\eta} \left(\left| \frac{dF}{d\eta} \right| \frac{dF}{d\eta} \right) \tag{3.41}$$

Step 3. Clearly, $y \to \infty$ corresponds to $\eta \to \infty$ and $y \to 0$ corresponds to $\eta \to 0$. Thus, the boundary conditions in Equations (3.30) and (3.31) transform to

$$F(\eta) \to 0 \quad \text{as} \quad \eta \to \infty \tag{3.42}$$

$$\frac{dF}{d\eta} = 0 \quad \text{at} \quad \eta = 0 \tag{3.43}$$

and the integral constraint becomes

$$\int_0^\infty F(\eta)\, d\eta = \frac{D}{2\rho U_\infty u_o \delta} \tag{3.44}$$

Step 4. In seeking a similarity solution, we are attempting to make a separation of variables. The two terms on the left-hand side of Equation (3.41) have coefficients that in general vary with x. Also, the right-hand side of Equation (3.44) is a function of x. **The condition for existence of the similarity solution is that these three coefficients be independent of x.** Thus, we require the following three conditions.

$$\frac{U_\infty \delta u_o'}{u_o^2} = a_1, \qquad \frac{U_\infty \delta'}{u_o} = a_2, \qquad \frac{D}{2\rho U_\infty u_o \delta} = 1 \tag{3.45}$$

The quantities a_1 and a_2 must, of course, be constant. Note that we could have introduced a third constant in the integral constraint, but it is unnecessary (we, in effect, absorb the third constant in δ). The solution to these three simultaneous equations is simply

$$\delta(x) = \sqrt{\frac{a_2 D x}{\rho U_\infty^2}} \tag{3.46}$$

$$u_o(x) = \frac{1}{2}\sqrt{\frac{D}{a_2 \rho x}} \tag{3.47}$$

$$a_1 = -a_2 \tag{3.48}$$

Step 5. Finally, we expect that $F(\eta)$ will have its maximum value on the axis, and then fall monotonically to zero approaching the freestream. If this is true, then $F'(\eta)$ will be negative for all values of η and we can replace its absolute value with $-F'(\eta)$. Taking account of Equations (3.45) through (3.48), the momentum equation now simplifies to

$$\alpha^2 \frac{d}{d\eta}\left[(F')^2\right] - a_2(\eta F' + F) = 0 \tag{3.49}$$

The second term is a perfect differential so that Equation (3.49) can be rewritten as

$$\frac{d}{d\eta}\left[\alpha^2(F')^2 - a_2\eta F\right] = 0 \tag{3.50}$$

Integrating once and imposing the symmetry condition at $\eta = 0$ [Equation (3.43)] yields

$$\alpha\frac{dF}{d\eta} = -\sqrt{a_2\eta F} \tag{3.51}$$

where we observe that $F'(\eta)$ is everywhere less than zero. Integrating once more, we find that the solution for $F(\eta)$ is

$$F(\eta) = C^2\left[1 - (\eta/\eta_e)^{3/2}\right]^2 \tag{3.52}$$

where C is a constant of integration and η_e is given by

$$\eta_e = (3\alpha C/\sqrt{a_2}\,)^{2/3} \tag{3.53}$$

This solution has a peak value at $\eta = 0$ and decreases monotonically to zero as $\eta \to \eta_e$. It then increases without limit for $\eta > \eta_e$. The only way we can satisfy the far field boundary condition [Equation (3.42)] is to use Equation (3.52) for $0 \leq \eta \leq \eta_e$ and to use the trivial solution, $F(\eta) = 0$, for values of η in excess of η_e.

With no loss of generality, we can set $\eta_e = 1$. To understand this, note that $\eta/\eta_e = y/[\eta_e\delta(x)]$. Hence, by setting $\eta_e = 1$ we simply rescale the η coordinate so that $\delta(x)$ is the wake half width as originally planned. Therefore,

$$3\alpha C = \sqrt{a_2} \tag{3.54}$$

Finally, imposing the integral constraint, Equation (3.44), yields an equation for the constant C. Performing the integration, we have

$$\int_0^1 C^2[1 - \eta^{3/2}]^2\, d\eta = \frac{9}{20}C^2 = 1 \tag{3.55}$$

Therefore,

$$C = \sqrt{20}/3 = 1.491 \tag{3.56}$$

and

$$\alpha = \sqrt{a_2/20} \tag{3.57}$$

If the closure coefficient α were known, our solution would be completely determined at this point with Equation (3.57) specifying a_2. This

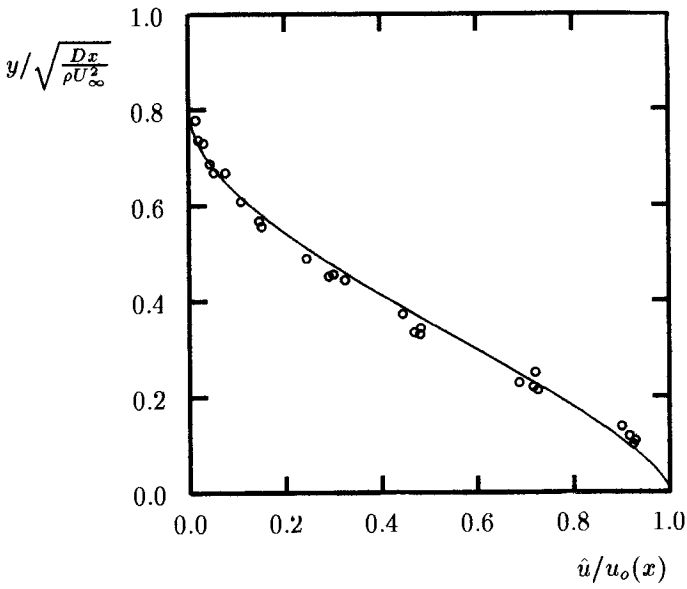

Figure 3.3: Comparison of computed and measured velocity profiles for the far wake; —— Mixing length; o Fage and Falkner.

is the nature of an **incomplete** turbulence model. The coefficient α is unknown because the mixing length [Equation (3.34)] is unknown a priori for this flow. To complete the solution, we appeal to experimental data [c.f. Schlichting (1979)], which show that the wake half width grows according to

$$\delta(x) \approx 0.805\sqrt{\frac{Dx}{\rho U_\infty^2}} \tag{3.58}$$

Comparison of Equations (3.46) and (3.58) shows that the value of a_2 is

$$a_2 = 0.648 \tag{3.59}$$

The value of the coefficient α then follows from Equation (3.57), i.e.,

$$\alpha = 0.18 \tag{3.60}$$

Collecting all of this, the final solution for the far wake, according to the mixing-length model is

$$U(x,y) = U_\infty - 1.38\sqrt{\frac{D}{\rho x}}\left[1 - (y/\delta)^{3/2}\right]^2 \tag{3.61}$$

where $\delta(x)$ is given by Equation (3.58). Figure 3.3 compares the theoretical profile with experimental data of Fage and Falkner (1932). As shown, the mixing-length model, once calibrated, does an excellent job of reproducing measured values. As a final comment, this solution has an interesting feature that we will see in many of our applications. Specifically, we have found a sharp turbulent/nonturbulent interface. This manifests itself in the nonanalytic behavior of the solution at $y/\delta = 1$, i.e., all derivatives of U above $\partial^2 U/\partial y^2$ are discontinuous at $y/\delta = 1$. Measurements confirm existence of such interfaces in all turbulent flows. However, the time-averaged interface is continuous to high order, being subjected to a near-Gaussian jitter. Time averaging would thus smooth out the sharpness of the physical interface. Consistent with this smoothing, we should actually expect analytical behavior approaching the freestream. Hence, the mixing-length model is predicting a nonphysical feature.

3.3.2 The Mixing Layer

For the mixing layer, we consider two parallel streams with velocities U_1 and U_2. By convention, the stream with velocity U_1 lies above $y = 0$ and $U_1 > U_2$. The boundary conditions are thus

$$U(x, y) \to U_1 \quad \text{as} \quad y \to +\infty \tag{3.62}$$

$$U(x, y) \to U_2 \quad \text{as} \quad y \to -\infty \tag{3.63}$$

The most convenient way to solve this problem is to introduce the streamfunction, ψ. The velocity components are given in terms of ψ as follows.

$$U = \frac{\partial \psi}{\partial y} \quad \text{and} \quad V = -\frac{\partial \psi}{\partial x} \tag{3.64}$$

Equation (3.23) is automatically satisfied and the momentum equation becomes

$$\frac{\partial \psi}{\partial y}\frac{\partial^2 \psi}{\partial x \partial y} - \frac{\partial \psi}{\partial x}\frac{\partial^2 \psi}{\partial y^2} = \frac{\partial}{\partial y}\left[\ell_{mix}^2 \left|\frac{\partial^2 \psi}{\partial y^2}\right| \frac{\partial^2 \psi}{\partial y^2}\right] \tag{3.65}$$

The boundary conditions on ψ are

$$\frac{\partial \psi}{\partial y} \to U_1 \quad \text{as} \quad y \to +\infty \tag{3.66}$$

$$\frac{\partial \psi}{\partial y} \to U_2 \quad \text{as} \quad y \to -\infty \tag{3.67}$$

Because the velocity is obtained from the streamfunction by differentiation, ψ involves a constant of integration. For the sake of uniqueness, we can specify an additional boundary condition on ψ, although at this point it is unclear where we should impose the extra boundary condition. The choice will become obvious when we set up the similarity solution. As with the far wake, we assume

$$\psi(x, y) = \psi_o(x)F(\eta) \tag{3.68}$$

where the similarity variable, η, is defined by

$$\eta = y/\delta(x) \tag{3.69}$$

As can be verified by substituting Equations (3.68) and (3.69) into Equation (3.65), a similarity solution exists provided we choose

$$\psi_o(x) = AU_1 x \tag{3.70}$$

$$\delta(x) = Ax \tag{3.71}$$

where A is a constant to be determined. Using Equation (3.34) to determine the mixing length, Equation (3.65) transforms to

$$\alpha^2 \frac{d}{d\eta}\left[(F'')^2\right] + AFF'' = 0 \tag{3.72}$$

Note that we have removed the absolute value sign in Equation (3.65) by noting that we expect a solution with $\partial U/\partial y = \partial^2\psi/\partial y^2 > 0$. As an immediate consequence, we can simplify Equation (3.72). Specifically, expanding the first term leads to the following **linear** equation for the transformed streamfunction, $F(\eta)$.

$$2\alpha^2 \frac{d^3F}{d\eta^3} + AF = 0 \tag{3.73}$$

To determine the constant of integration in the streamfunction, note that our assumed form for ψ [Equation (3.68)] is consistent with letting $F(\eta)$ vanish at $\eta = 0$. This is known as the dividing streamline. Thus, our boundary conditions are

$$\frac{dF}{d\eta} \to 1 \quad \text{as} \quad \eta \to +\infty \tag{3.74}$$

$$\frac{dF}{d\eta} \to U_2/U_1 \quad \text{as} \quad \eta \to -\infty \tag{3.75}$$

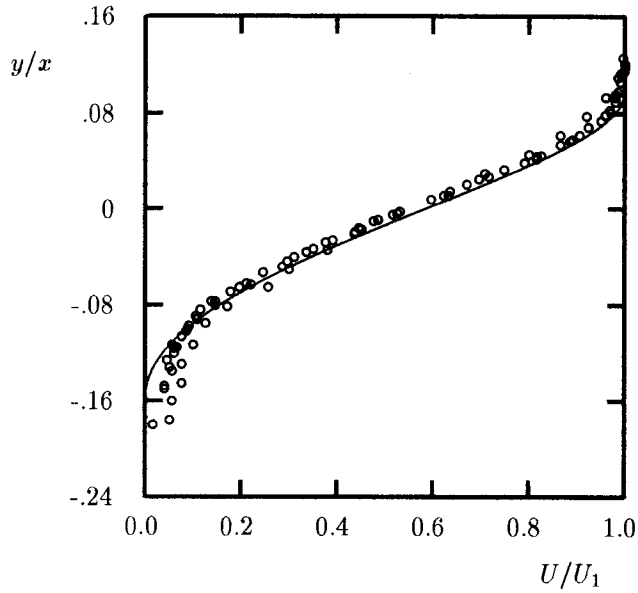

Figure 3.4: Comparison of computed and measured velocity profiles for a mixing layer; —— Mixing length; o Liepmann and Laufer.

$$F(0) = 0 \tag{3.76}$$

For simplicity, we consider the limiting case $U_2 = 0$. This problem can be solved in closed form using elementary methods. Unfortunately, the solution is a bit complicated. Furthermore, as with the far-wake solution, the mixing-length model predicts a sharp turbulent/nonturbulent interface and it becomes a rather difficult chore to determine a straightforward relationship between the closure coefficient α and the constant A. The easier way to proceed is to solve the equation numerically for various values of α^2/A and compare with experimental measurements to infer the values of α and A. Proceeding in this manner (see Program MIXER in Appendix C), optimum agreement between computed and measured [Liepmann and Laufer (1947)] velocity profiles occurs if we choose

$$A = 0.247 \quad \text{and} \quad \alpha = 0.071 \quad \text{(Mixing Layer)} \tag{3.77}$$

This value of α is nearly identical to the value (0.070) quoted by Launder and Spalding (1972). Figure 3.4 compares computed and measured velocity profiles. The traditional definition of spreading rate, C_δ, for the mixing

layer is the difference between the values of y/x where $(U-U_2)^2/(U_1-U_2)^2$ is 9/10 and 1/10. The values of A and α have been selected to match the experimentally measured spreading rate, viz.,

$$C_\delta = 0.115 \tag{3.78}$$

While the computed velocity goes to zero more rapidly than measured on the low speed side of the mixing layer, the overall agreement between theory and experiment is remarkably good.

3.3.3 The Jet

We now analyze the two-dimensional, or **plane jet**, and the axisymmetric, or **round jet**. Referring to Figure 3.2(c), we assume the jet issues into a stagnant fluid. The jet entrains fluid from the surrounding fluid and grows in width downstream of the origin. Equations (3.23) and (3.24) govern the motion with $j = 0$ corresponding to the plane jet and $j = 1$ corresponding to the round jet. As with the far wake, we take advantage of the symmetry about the x axis and solve for $0 \leq y < \infty$. The boundary conditions for both the plane and the round jet are

$$U(x,y) \to 0 \quad \text{as} \quad y \to \infty \tag{3.79}$$

$$\frac{\partial U}{\partial y} = 0 \quad \text{at} \quad y = 0 \tag{3.80}$$

To insure that the momentum in the jet is conserved, our solution must satisfy the following integral constraint:

$$\pi^j \int_0^\infty U^2 y^j \, dy = \frac{1}{2} J \tag{3.81}$$

where J is the momentum flux per unit mass, or, **specific momentum flux**.

To solve, we introduce the streamfunction, which can be generalized to account for the axisymmetry of the round jet, i.e.,

$$y^j U = \frac{\partial \psi}{\partial y} \quad \text{and} \quad y^j V = -\frac{\partial \psi}{\partial x} \tag{3.82}$$

The momentum equation thus becomes

$$\begin{aligned} y^{-j} \frac{\partial \psi}{\partial y} \frac{\partial^2 \psi}{\partial x \partial y} \quad - \quad & \frac{\partial \psi}{\partial x} \frac{\partial}{\partial y} \left(y^{-j} \frac{\partial \psi}{\partial y} \right) \\ = \quad & \frac{\partial}{\partial y} \left[y^j \ell_{mix}^2 \left| \frac{\partial}{\partial y} \left(y^{-j} \frac{\partial \psi}{\partial y} \right) \right| \frac{\partial}{\partial y} \left(y^{-j} \frac{\partial \psi}{\partial y} \right) \right] \end{aligned} \tag{3.83}$$

Assuming a similarity solution of the form given in Equations (3.68) and (3.69), the appropriate forms for $\psi_o(x)$ and $\delta(x)$ are

$$\psi_o(x) = \sqrt{\frac{JA^{j+1}x^{j+1}}{2\pi^j}} \tag{3.84}$$

$$\delta(x) = Ax \tag{3.85}$$

where A is a constant that will be determined by comparison with experimental data. For the jet, we expect to have $\partial U/\partial y \leq 0$. Using this fact to replace the absolute value in Equation (3.83) with a minus sign, the following ordinary differential equation for the transformed streamfunction, $F(\eta)$, results.

$$\alpha^2\eta^j \left[\frac{d}{d\eta}\left(\frac{F'}{\eta^j}\right)\right]^2 = \frac{j+1}{2}AF\left(\frac{F'}{\eta^j}\right) \tag{3.86}$$

This equation must be solved subject to the following conditions.

$$F(0) = 0 \tag{3.87}$$

$$\frac{1}{\eta^j}\frac{dF}{d\eta} \to 0 \quad \text{as} \quad y \to \infty \tag{3.88}$$

$$\frac{d}{d\eta}\left[\frac{1}{\eta^j}\frac{dF}{d\eta}\right] \quad \text{as} \quad y \to 0 \tag{3.89}$$

$$\int_0^\infty \frac{(F')^2}{\eta^j}\, d\eta = 1 \tag{3.90}$$

Performing a numerical solution of Equation (3.86) subject to Equations (3.87) through (3.90), and comparing with experiment yields

$$A = 0.246 \quad \text{and} \quad \alpha = 0.098 \quad \text{(Plane Jet)} \tag{3.91}$$

$$A = 0.233 \quad \text{and} \quad \alpha = 0.080 \quad \text{(Round Jet)} \tag{3.92}$$

The values for α are about 8% larger than corresponding values (0.090 and 0.075) quoted by Launder and Spalding (1972). The Launder-Spalding results were obtained using numerical procedures of the 1960's and are unlikely to be free of numerical error. By contrast, the values quoted in Equations (3.91) and (3.92) have been obtained using an accurate solver (see Program JET in Appendix C). Figures 3.5 and 3.6 compare computed and measured [Wygnanski and Fiedler (1968), Bradbury (1965)] velocity profiles for the plane and round jets. Somewhat larger discrepancies between theory and experiment are present for the plane jet than for the round jet.

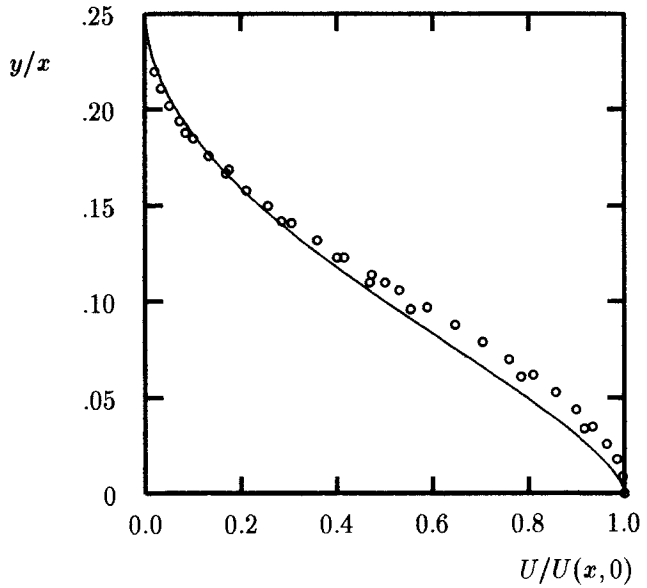

Figure 3.5: Comparison of computed and measured velocity profiles for the plane jet; —— Mixing length; o Wygnanski and Fiedler.

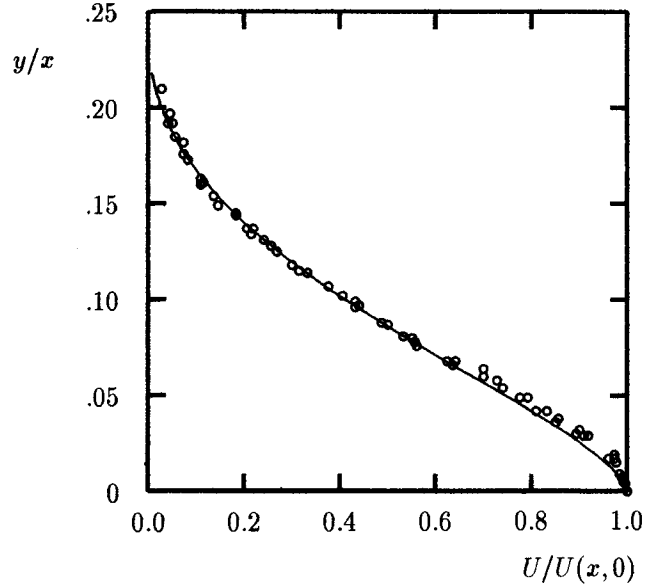

Figure 3.6: Comparison of computed and measured velocity profiles for the round jet; —— Mixing length; o Bradbury.

The traditional definition of spreading rate, C_δ, for the jet is the value of y/x where the velocity is half its peak value. Experimental data indicate C_δ is between 0.100 and 0.110 for the plane jet and between 0.086 and 0.095 for the round jet. The mixing-length computational results shown in Figures 3.5 and 3.6 correspond to

$$C_\delta = \begin{cases} 0.100 & \text{(Plane Jet)} \\ 0.086 & \text{(Round Jet)} \end{cases} \tag{3.93}$$

This concludes our application of the mixing-length model to free shear flows. A few final comments will help put this model into proper perspective. We postulated in Equation (3.34) that the mixing length is proportional to the width of the shear layer. Our theory thus has a single **closure coefficient**, α, and we have found that it must be changed for each flow. The following values are optimum for the four cases considered.

Far Wake	$\alpha = 0.180$
Mixing Layer	$\alpha = 0.071$
Plane Jet	$\alpha = 0.098$
Round Jet	$\alpha = 0.080$

While fairly close agreement has been obtained between computed and measured velocity profiles, we have not predicted the all important spreading rate. In fact, we established the value of our closure coefficient by forcing agreement with the measured spreading rate. If we are only interested in far-wake applications or round jets we might use this model with the appropriate closure coefficient for a parametric study in which some flow property might be varied. However, we must proceed with some degree of trepidation knowing that our formulation lacks in universality.

3.4 Modern Variants of the Mixing-Length Model

For free shear flows, we have seen that the mixing length is constant across the layer and proportional to the width of the layer. For flow near a solid boundary, turbulence behaves differently and, not too surprisingly, we must use a different prescription for the mixing length. Prandtl originally postulated that for flows near solid boundaries the mixing length is proportional to the distance from the surface. As we will demonstrate shortly, this postulate is consistent with the well-known **law of the wall**, which has been observed for a wide range of wall-bounded flows.

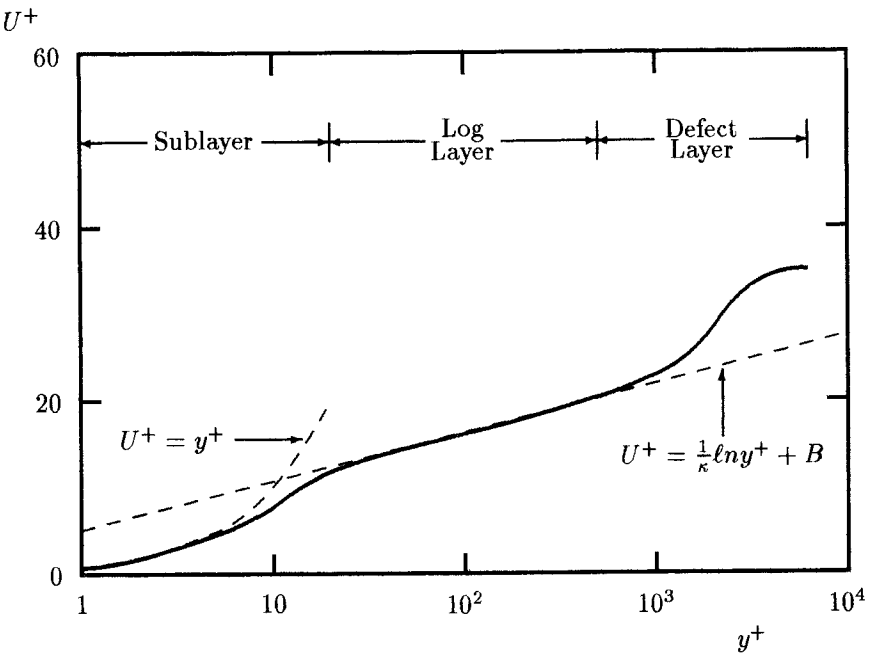

Figure 3.7: Typical velocity profile for a turbulent boundary layer.

Figure 3.7 shows a typical velocity profile for a turbulent boundary layer. The quantity y^+, which will be defined below [Equation (3.101)], is dimensionless distance from the surface. From an experimenter's point of view, three distinct regions are discernible, viz., the **viscous sublayer**, the **log layer** and the **defect layer**. By definition, the log layer, sometimes referred to as the "fully turbulent wall layer," is the portion of the boundary layer sufficiently close to the surface that inertial terms can be neglected yet sufficiently distant that the molecular, or viscous, stress is negligible compared to the Reynolds stress. This region typically lies between $y^+ = 30$ and $y = 0.1\delta$, where the upper boundary is dependent upon Reynolds number. Of particular interest to the present discussion, the **law of the wall** holds in the log layer. The viscous sublayer is the region between the surface and the log layer. Close to the surface, the velocity varies approximately linearly with y^+, and gradually asymptotes to the law of the wall for large values of y^+. The defect layer lies between the log layer and the edge of the boundary layer. The velocity asymptotes to the law of the wall as $y/\delta \rightarrow 0$, and makes a noticeable departure from the law of the

wall approaching the freestream. Chapter 4 discusses these three layers in great detail.

From a mathematician's point of view, there are actually only two layers, viz., the viscous sublayer and the defect layer. In the parlance of singular perturbation theory (Appendix B), the defect layer is the region in which the outer expansion is valid, while the viscous sublayer is the region where the inner expansion holds. In performing the classical matching procedure, we envision the existence of an overlap region, in which both the viscous sublayer and defect-layer solutions are valid. In the present context, we choose to call the overlap region the log layer. Strictly speaking, the log layer is not a distinct layer, but rather the asymptotic limit of the inner and outer layers. Nevertheless, we will find the log layer to be useful because of the simplicity of the equations of motion in the layer .

Consider a constant-pressure boundary layer. The flow is governed by the standard boundary-layer equations.

$$\frac{\partial U}{\partial x} + \frac{\partial V}{\partial y} = 0 \tag{3.94}$$

$$\rho U \frac{\partial U}{\partial x} + \rho V \frac{\partial U}{\partial y} = \frac{\partial}{\partial y}\left[\mu \frac{\partial U}{\partial y} + \tau_{xy}\right] \tag{3.95}$$

Because the convective terms are negligible in the log layer, the sum of the viscous and Reynolds shear stress must be constant. Hence, we can say

$$\mu \frac{\partial U}{\partial y} + \tau_{xy} \approx \mu \left(\frac{\partial U}{\partial y}\right)_w = \tau_w = \rho u_\tau^2 \tag{3.96}$$

where subscript w denotes value at the wall and $u_\tau = \sqrt{\tau_w/\rho}$ is known as the **friction velocity**. As noted above, the Reynolds stress is much larger than the viscous stress in the log layer. Consequently, according to the mixing-length model,

$$\ell_{mix}^2 \left(\frac{\partial U}{\partial y}\right)^2 \approx u_\tau^2 \tag{3.97}$$

If we say that the mixing length is given by

$$\ell_{mix} = \kappa y \tag{3.98}$$

where κ is a constant, Equation (3.97) can be integrated immediately to yield

$$U \approx \frac{u_\tau}{\kappa} \ell n\, y + \text{constant} \tag{3.99}$$

This equation assumes a more familiar form when we introduce the dimensionless velocity and normal distance defined by

$$U^+ = U/u_\tau \tag{3.100}$$

$$y^+ = u_\tau y/\nu \tag{3.101}$$

Introducing Equations (3.100) and (3.101) into Equation (3.99) yields the classical **law of the wall**, viz.,

$$U^+ \approx \frac{1}{\kappa} \ell n\, y^+ + B \tag{3.102}$$

The coefficient κ is known as the **Kármán constant**, and B is a dimensionless constant. Coles and Hirst (1969) found from correlation of experimental data for a large number of attached, incompressible boundary layers with and without pressure gradient that

$$\kappa \approx 0.41 \tag{3.103}$$

$$B \approx 5.0 \tag{3.104}$$

Note that this is not intended as a derivation of the law of the wall. Rather, it simply illustrates consistency of Equation (3.98) with the law of the wall.

Using Equation (3.98) all the way from $y = 0$ to $y = \delta$, the mixing-length model fails to provide close agreement with measured skin friction for boundary layers. Of course, not even Prandtl expected that $\ell_{mix} = \kappa y$ throughout the boundary layer. Since the mixing length was first postulated, considerable effort has been made aimed at finding a suitable prescription for boundary-layer computations. Several key modifications to Equation (3.98) have evolved, three of which deserve our immediate attention. See Schlichting (1979) or Hinze (1975) for a more-complete history of the mixing-length model's evolution.

The first key modification was devised by Van Driest (1956) who proposed that the mixing length should be multiplied by a damping function. Specifically, Van Driest proposed, with some theoretical support but mainly as a good fit to data, that the mixing length should behave according to

$$\ell_{mix} = \kappa y \left[1 - e^{-y^+/A_o^+}\right] \tag{3.105}$$

where the constant A_o^+ is

$$A_o^+ = 26 \tag{3.106}$$

Aside from the primary need to improve predictive accuracy, the Van Driest modification improves our description of the Reynolds stress in the

limit $y \to 0$. With ℓ_{mix} given by Equation (3.98), the Reynolds shear stress $\tau_{xy} \sim y^2$ as $y \to 0$. However, the no-slip boundary condition tells us that $u' = 0$ at $y = 0$. Since there is no a priori reason for $\partial u'/\partial y$ to vanish at the surface, we conclude that $u' \sim y$ as $y \to 0$. Since the fluctuating velocity satisfies the continuity equation, we also conclude that $v' \sim y^2$. Hence, the Reynolds shear stress must go to zero as y^3. Results of DNS studies (Chapter 8) indicate that indeed $\tau_{xy} \sim y^3$ as $y \to 0$. However, as noted by Hinze (1975), the coefficient of the y^3 term in a Taylor series expansion for τ_{xy} must be very small as measurements are as close to $\tau_{xy} \sim y^4$ as they are to $\tau_{xy} \sim y^3$ when $y \to 0$. In the limit of small y the Van Driest mixing length implies τ_{xy} goes to zero as y^4 approaching the surface.

The second key modification was made by Clauser (1956) who addressed the proper form of the eddy viscosity in the defect layer. In analogy to Prandtl's special form of the eddy viscosity for wake flows given in Equation (3.25), Clauser specifies that

$$\mu_{T_o} = \alpha \rho U_e \delta^* \tag{3.107}$$

where μ_{T_o} is the eddy viscosity in the outer part of the layer, δ^* is the displacement thickness, U_e is the velocity at the edge of the layer, and α is a closure coefficient.

In a similar vein, Escudier (1966) found that predictive accuracy is improved by limiting the peak value of the mixing length according to

$$(\ell_{mix})_{max} = 0.09\delta \tag{3.108}$$

where δ is boundary-layer thickness. Escudier's modification is the same approximation we used in analyzing free shear flows [Equation (3.34)], although the value 0.09 is half the value we found for the far wake.

Using an eddy viscosity appropriate to wake flow in the outer portion of the boundary layer also improves our physical description of the turbulent boundary layer. Measurements indeed indicate that the turbulent boundary layer exhibits wake-like characteristics in the defect layer. As pointed out by Coles and Hirst (1969), **"a typical boundary layer flow can be viewed as a wake-like structure which is constrained by a wall."** Figure 3.8 illustrates Coles' notion that the defect layer resembles a wake flow while the wall constraint is felt primarily in the sublayer and log layer. Strictly speaking, turbulence structure differs a lot between a boundary layer and a wake. Hence, the terminology "wake component" is conceivably a bit misleading from a conceptual point of view. Nevertheless, the mathematical approximations that yield accurate predictions for a wake and for the outer portion of a turbulent boundary layer are remarkably similar.

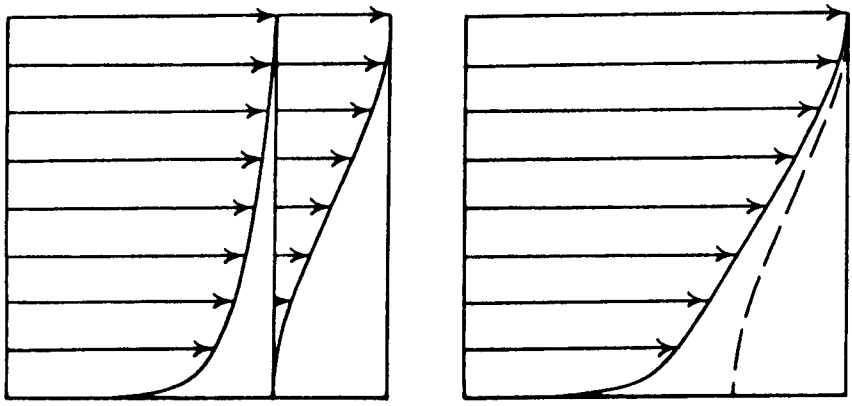

Figure 3.8: Coles' description of the turbulent boundary layer. [From Coles and Hirst (1969) — Used with permission.]

The third key modification is due to Corrsin and Kistler (1954) and Klebanoff (1956) as a corollary result of their experimental studies of **intermittency**. They found that approaching the freestream from within the boundary layer, the flow is not always turbulent. Rather, it is sometimes laminar and sometimes turbulent, i.e., it is **intermittent**. Their measurements indicate that for smooth walls, the eddy viscosity should be multiplied by

$$F_{Kleb}(y;\delta) = \left[1 + 5.5\left(\frac{y}{\delta}\right)^6\right]^{-1} \tag{3.109}$$

where δ is the boundary-layer thickness. This provides a measure of the effect of intermittency on the flow.

All of these modifications have evolved as a result of the great increase in power and accuracy of computing equipment and experimental measurement techniques since the 1940's. The next two subsections introduce the two most noteworthy models in use today that are based on the mixing-length concept. Both include variants of the Van Driest, Clauser, and Klebanoff modifications. Although it is not used in these two models, the Escudier modification has also enjoyed great popularity.

As a final comment, we have introduced two new closure coefficients, A_o^+ and α, and an empirical function, F_{Kleb}. As we continue in our journey through this book, we will find that the number of such coefficients increases as we attempt to describe more and more features of the turbulence.

3.4.1 Cebeci-Smith Model

The Cebeci-Smith model [Smith and Cebeci (1967)] is a two-layer model with μ_T given by separate expressions in each layer. The eddy viscosity is

$$\mu_T = \begin{cases} \mu_{T_i}, & y \le y_m \\ \mu_{T_o}, & y > y_m \end{cases} \tag{3.110}$$

where y_m is the smallest value of y for which $\mu_{T_i} = \mu_{T_o}$. The values of μ_T in the inner layer, μ_{T_i}, and the outer layer, μ_{T_o}, are computed as follows.

Inner Layer:

$$\mu_{T_i} = \rho \ell_{mix}^2 \left[\left(\frac{\partial U}{\partial y} \right)^2 + \left(\frac{\partial V}{\partial x} \right)^2 \right]^{1/2} \tag{3.111}$$

$$\ell_{mix} = \kappa y \left[1 - e^{-y^+/A^+} \right] \tag{3.112}$$

Outer layer:

$$\mu_{T_o} = \alpha \rho U_e \delta_v^* F_{Kleb}(y; \delta) \tag{3.113}$$

Closure Coefficients:

$$\kappa = 0.40, \qquad \alpha = 0.0168, \qquad A^+ = 26 \left[1 + y \frac{dP/dx}{\rho u_\tau^2} \right]^{-1/2} \tag{3.114}$$

The function F_{Kleb} is the Klebanoff intermittency function given by Equation (3.109), U_e is boundary-layer edge velocity, and δ_v^* is the **velocity thickness** defined by

$$\delta_v^* = \int_0^\delta (1 - U/U_e)\, dy \tag{3.115}$$

Note that velocity thickness is identical to displacement thickness for incompressible flow. The coefficient A^+ differs from Van Driest's value to improve predictive accuracy for boundary layers with nonzero pressure gradient. The prescription for μ_{T_i} above is appropriate only for two-dimensional flows; for three-dimensional flows, it should be proportional to a quantity such as the magnitude of the vorticity vector. There are many other subtle modifications to this model for specialized applications including surface mass transfer, streamline curvature, surface roughness, low Reynolds number, etc. Cebeci and Smith (1974) give complete details of their model with all its variations.

The Cebeci-Smith model is especially elegant and easy to implement. Most of the computational effort, relative to a laminar case, goes into computing the velocity thickness. This quantity is readily available in boundary-layer computations so that a laminar flow program can usually be converted to a turbulent flow program with just a few extra lines of instructions. Figure 3.9 illustrates a typical eddy viscosity profile constructed by using μ_{T_i} between $y = 0$ and $y = y_m$, and μ_{T_o} for the rest of the layer. At Reynolds numbers typical of fully-developed turbulence, matching between the inner and outer layers will occur well into the log layer.

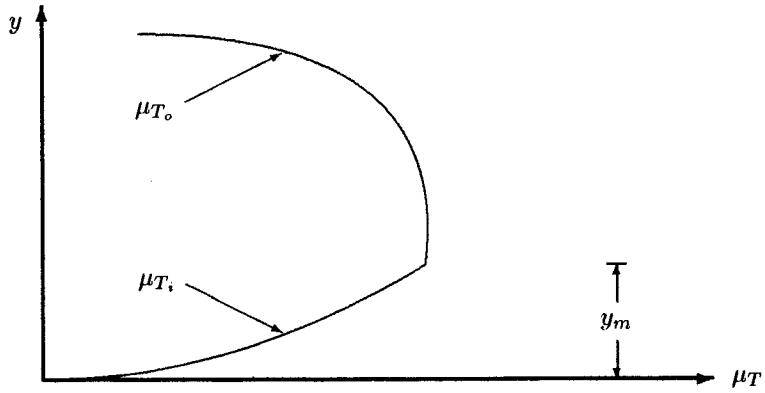

Figure 3.9: Eddy viscosity for the Cebeci-Smith model.

We can estimate the value of y_m^+ as follows. Since we expect the matching point to lie well within the log layer, the exponential term in the Van Driest damping function will be negligible. Also, the law of the wall [Equation (3.99)] tells us $\partial U/\partial y \approx u_\tau/(\kappa y)$. Thus,

$$\mu_{T_i} \approx \rho\kappa^2 y^2 \frac{u_\tau}{\kappa y} \approx \rho\kappa u_\tau y = \kappa\mu y^+ \tag{3.116}$$

Since the matching point also lies close enough to the surface that we can say $y/\delta \ll 1$, the Klebanoff intermittency function will be close to one so that (with $\delta_v^* = \delta^*$):

$$\mu_{T_o} \approx \alpha\rho U_e \delta^* = \alpha\mu Re_{\delta^*} \tag{3.117}$$

Hence, equating μ_{T_i} and μ_{T_o}, we find that

$$y_m^+ \approx \frac{\alpha}{\kappa} Re_{\delta^*} \approx 0.04 Re_{\delta^*} \tag{3.118}$$

Assuming a typical turbulent boundary layer for which $Re_{\delta^*} \sim 10^4$, the matching point will lie at $y_m^+ \sim 400$.

3.4.2 Baldwin-Lomax Model

The Baldwin-Lomax model [Baldwin and Lomax (1978)] was formulated for use in computations where boundary-layer properties such as δ, δ_v^* and U_e are difficult to determine. This situation often arises in numerical simulation of separated flows, especially for flows with shock waves. Like the Cebeci-Smith model, this is a two-layer model. The eddy viscosity is given by Equation (3.110), and the inner and outer layer viscosities are as follows:

Inner Layer:

$$\mu_{T_i} = \rho \ell_{mix}^2 |\omega| \tag{3.119}$$

$$\ell_{mix} = \kappa y \left[1 - e^{-y^+/A_o^+}\right] \tag{3.120}$$

Outer Layer:

$$\mu_{T_o} = \rho \alpha C_{cp} F_{wake} F_{Kleb}(y; y_{max}/C_{Kleb}) \tag{3.121}$$

$$F_{wake} = \min\left[y_{max} F_{max}; C_{wk} y_{max} U_{dif}^2 / F_{max}\right] \tag{3.122}$$

$$F_{max} = \frac{1}{\kappa}\left[\max_y(\ell_{mix}|\omega|)\right] \tag{3.123}$$

where y_{max} is the value of y at which $\ell_{mix}|\omega|$ achieves its maximum value.

Closure Coefficients:

$$\left.\begin{array}{lll} \kappa = 0.40, & \alpha = 0.0168, & A_o^+ = 26 \\ C_{cp} = 1.6, & C_{Kleb} = 0.3, & C_{wk} = 1 \end{array}\right\} \tag{3.124}$$

The function F_{Kleb} is Klebanoff's intermittency function [Equation (3.109)] with δ replaced by y_{max}/C_{Kleb}, and ω is the magnitude of the vorticity vector, i.e.,

$$\omega = \left[\left(\frac{\partial V}{\partial x} - \frac{\partial U}{\partial y}\right)^2 + \left(\frac{\partial W}{\partial y} - \frac{\partial V}{\partial z}\right)^2 + \left(\frac{\partial U}{\partial z} - \frac{\partial W}{\partial x}\right)^2\right]^{1/2} \tag{3.125}$$

for fully three-dimensional flows. This simplifies to $\omega = |\partial V/\partial x - \partial U/\partial y|$ in a two-dimensional flow. If the boundary layer approximations are used in a two-dimensional flow, then $\omega = |\partial U/\partial y|$.

U_{dif} is the maximum value of U for boundary layers. For free shear layers, U_{dif} is the difference between the maximum velocity in the layer and the value of U at $y = y_{max}$.

The primary difference between the Baldwin-Lomax and Cebeci-Smith models is in the outer layer, where the product $C_{cp}F_{wake}$ replaces $U_e\delta_v^*$. To avoid the need to locate the boundary-layer edge, the Baldwin-Lomax model establishes the outer-layer length scale in terms of the vorticity in the layer. On the one hand, using $F_{wake} = y_{max}F_{max}$, we in effect replace δ_v^* by $y_{max}^2\omega/U_e$. On the other hand, using $F_{wake} = C_{wk}y_{max}U_{dif}^2/F_{max}$ effectively replaces the shear layer width, δ, in Prandtl's eddy-viscosity model [Equation (3.25)] by $U_{dif}/|\omega|$.

As a final comment, while Equation (3.124) implies this model has six closure coefficients, there are actually only five. The coefficient C_{cp} appears only in Equation (3.121) where it is multiplied by α, so αC_{cp} can be treated as a single constant.

3.5 Application to Wall-Bounded Flows

We turn our attention now to application of the Cebeci-Smith and Baldwin-Lomax models to wall-bounded flows, i.e., to flows with a solid boundary. The no-slip boundary condition must be enforced for wall-bounded flows, and we expect to find a viscous layer similar to that depicted in Figure 3.7. This Section first examines two internal flows, viz., channel flow and pipe flow. Then, we consider external flows, i.e., boundary layers growing in a semi-infinite medium.

3.5.1 Channel and Pipe Flow

Like the free shear flow applications of Section 3.3, constant-section channel and pipe flow are excellent building-block cases for testing a turbulence model. Although we have the added complication of a solid boundary, the motion can be described with ordinary differential equations and is therefore easy to analyze mathematically. Also, experimental data are abundant for these flows.

The classical problems of flow in a channel, or duct, and a pipe are the idealized case of an infinitely long channel or pipe (Figure 3.10). This approximation is appropriate provided we are not too close to the inlet of the channel/pipe so that the flow has become **fully-developed**. For turbulent flow in a pipe, flow becomes fully developed approximately 50 pipe diameters downstream of the inlet. Because, by definition, properties no longer vary with distance along the channel/pipe, we conclude immediately that

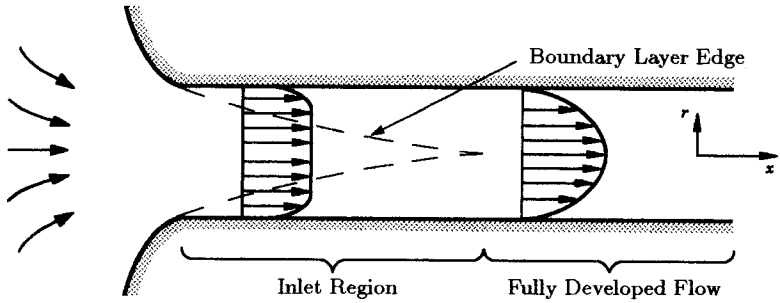

Figure 3.10: Fully-developed flow in a channel or pipe.

$$\frac{\partial \mathbf{U}}{\partial x} = \mathbf{0} \tag{3.126}$$

Denoting distance from the center of the channel or pipe by r, conservation of mass is

$$\frac{\partial U}{\partial x} + \frac{1}{r^j}\frac{\partial}{\partial r}\left[r^j V\right] = 0 \tag{3.127}$$

where $j = 0$ for channel flow and $j = 1$ for pipe flow. In light of Equation (3.126), we see that V does not vary across the channel/pipe. Since V must vanish at the channel/pipe walls, we conclude that $V = 0$ throughout the fully-developed region. Hence, for both channel and pipe flow, the inertial terms are exactly zero, so that the momentum equation simplifies to

$$0 = -\frac{dP}{dx} + \frac{1}{r^j}\frac{d}{dr}\left[r^j\left(\mu\frac{dU}{dr} + \tau_{xr}\right)\right] \tag{3.128}$$

In fully-developed flow pressure gradient must be independent of x and if $V = 0$ it is also exactly independent of y. Hence, we can integrate once to obtain

$$\mu\frac{dU}{dr} + \tau_{xr} = \frac{r}{j+1}\frac{dP}{dx} \tag{3.129}$$

Now, the Reynolds stress vanishes at the channel/pipe walls and this establishes a direct relationship between the pressure gradient and the shear stress at the walls. If we let R denote the half-height of the channel or the radius of the pipe, applying Equation (3.129) at $r = R$ tells us that

$$\tau_w = -\frac{R}{j+1}\frac{dP}{dx} \tag{3.130}$$

Hence, introducing the friction velocity, u_τ, the momentum equation for channel/pipe flow simplifies to the following first-order, ordinary differential equation.

$$\mu \frac{dU}{dr} + \tau_{xr} = -\rho u_\tau^2 \frac{r}{R} \tag{3.131}$$

Noting that both channel and pipe flow are symmetric about the centerline, we can obtain the complete solution by solving Equation (3.131) with r varying between 0 and R. It is more convenient however to define y as the distance from the wall so that

$$y = R - r \tag{3.132}$$

Hence, representing the Reynolds stress in terms of the eddy viscosity, μ_T, we arrive at the following equation for the velocity.

$$(\mu + \mu_T)\frac{dU}{dy} = \rho u_\tau^2 \left(1 - \frac{y}{R}\right) \tag{3.133}$$

Finally, we introduce sublayer coordinates, U^+ and y^+ from Equations (3.100) and (3.101), as well as $\mu_T^+ = \mu_T/\mu$. This results in the dimensionless form of the momentum equation for channel flow and pipe flow, viz.,

$$(1 + \mu_T^+)\frac{dU^+}{dy^+} = \left(1 - \frac{y^+}{R^+}\right) \tag{3.134}$$

where

$$R^+ = u_\tau R/\nu \tag{3.135}$$

Equation (3.134) must be solved subject to the no-slip boundary condition at the channel/pipe wall. Thus, we require

$$U^+(0) = 0 \tag{3.136}$$

At first glance, this appears to be a standard initial value problem that can, in principle, be solved using an integration scheme such as the Runge-Kutta method. However, the problem is a bit more difficult, and we find that for both the Cebeci-Smith and Baldwin-Lomax models, the problem must be solved iteratively. That is, for the Cebeci-Smith model, we don't know U_e and δ_v^* a priori. Similarly, with the Baldwin-Lomax model we don't know the values of U_{dif} and y_{max} until we have determined the entire velocity profile. This is not a serious complication however, and the solution can be obtained after just a few iterations.

The equations for channel and pipe flow can be conveniently solved using a standard over-relaxation iterative procedure. Appendix C describes a

program called PIPE that yields a numerical solution for several turbulence models, including the Cebeci-Smith and Baldwin-Lomax models.

Figure 3.11 compares computed two-dimensional channel-flow profiles with direct numerical simulation (DNS) results of Mansour, Kim and Moin (1988) for Reynolds number based on channel height and average velocity of 13,750. As shown, the Cebeci-Smith and Baldwin-Lomax velocity profiles are within 8% and 5%, respectively, of the DNS profiles. Computed Reynolds shear stress profiles for both models differ from the DNS profiles by no more than 2%. Computed skin friction for both models differs by less than 2% from Halleen and Johnston's (1967) correlation of experimental data, viz.,

$$c_f = 0.0706 Re_H^{-1/4} \tag{3.137}$$

where the skin friction and Reynolds number are based on the average velocity across the channel and the channel height H, i.e., $c_f = \tau_w/(\frac{1}{2}\rho U_{avg}^2)$ and $Re_H = U_{avg} H/\nu$.

Figure 3.12 compares model predicted pipe-flow properties with the experimental data of Laufer (1952) for a Reynolds number based on pipe diameter and average velocity of 40,000. Baldwin-Lomax velocity and Reynolds shear stress differ from measured values by no more than 3%. As with channel flow, the Cebeci-Smith velocity shows greater differences (8%) from the data. Computed skin friction is within 7% and 1% for the Cebeci-Smith and Baldwin-Lomax models, respectively, of Prandtl's universal law of friction for smooth pipes [see Schlichting (1979)] given by

$$\frac{1}{\sqrt{c_f}} = 4\, log_{10}\left(2 Re_D \sqrt{c_f}\right) - 1.6 \tag{3.138}$$

where c_f and Re_D are based on average velocity across the pipe and pipe diameter, D.

These computations illustrate that subtle differences in the Reynolds shear stress can lead to much larger differences in velocity for pipe and channel flow. This means we must determine the Reynolds shear stress very accurately in order to obtain accurate velocity profiles. To some extent this seems odd. The Reynolds stress is a higher-order correlation while velocity is a simple time average. Our natural expectation is for the mean velocity to be determined with great precision while higher-order quantities such as Reynolds stress are determined with a bit less precision. The dilemma appears to stem from the fact that we need the same precision in τ_{xy} as in $\partial U/\partial y$. As we advance to more complicated turbulence models, we will see this accuracy dilemma repeated, although generally with less severity. As applications go, channel and pipe flow are not very forgiving.

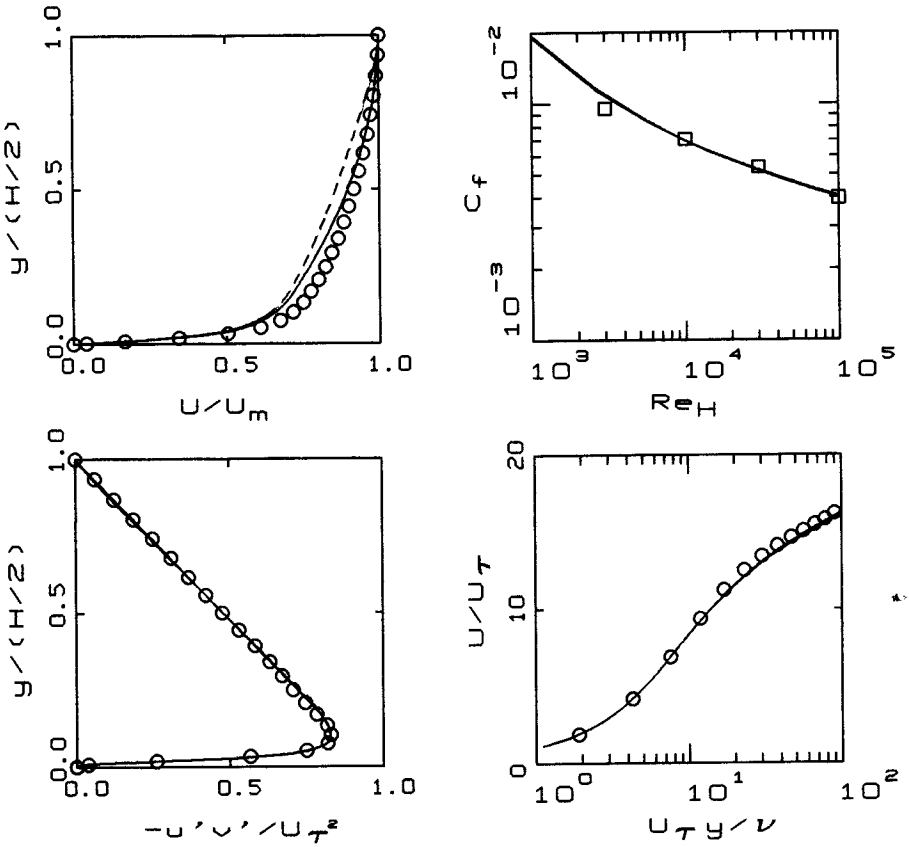

Figure 3.11: Comparison of computed and measured channel-flow properties, $Re_H = 13{,}750$. —— Baldwin-Lomax; - - - Cebeci-Smith; o Mansour et al. (DNS); □ Halleen-Johnston correlation.

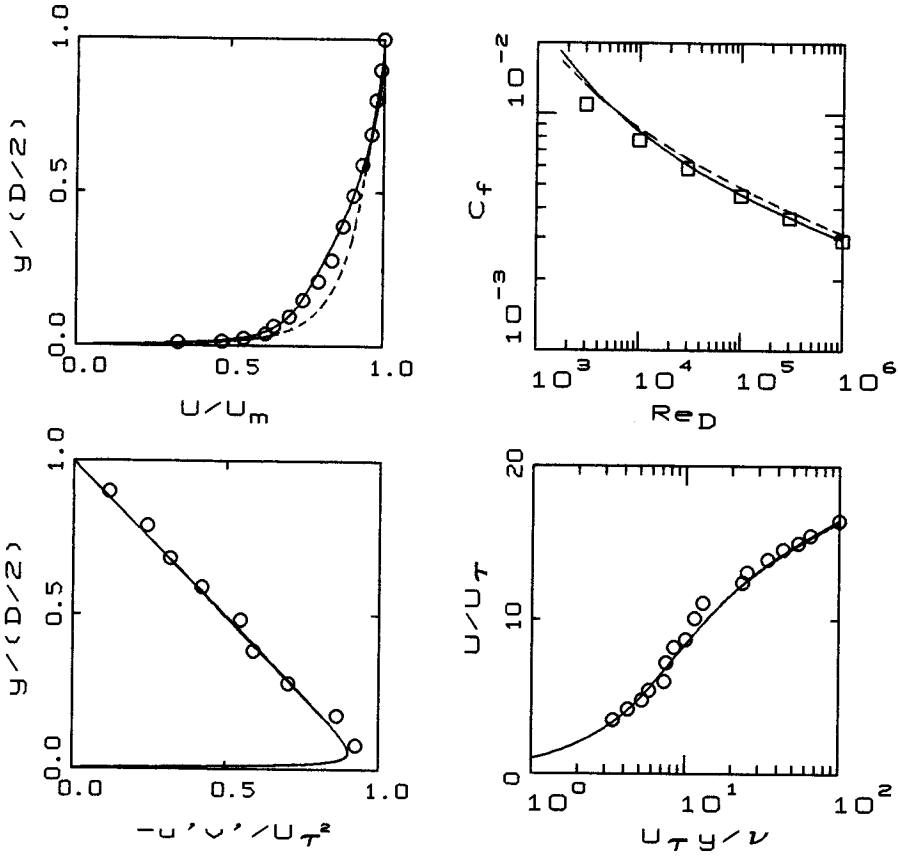

Figure 3.12: Comparison of computed and measured pipe-flow properties, $Re_D = 40{,}000$. —— Baldwin-Lomax; - - - Cebeci-Smith; o Laufer; □ Prandtl correlation.

Interestingly, for the higher Reynolds number pipe flow, more acceleration is predicted with the Cebeci-Smith model than with the Baldwin-Lomax model. The opposite is true for the lower Reynolds number channel-flow case. Cebeci and Smith (1974) have devised low-Reynolds-number corrections for their model which, presumably, would reduce the differences from the DNS channel-flow results.

3.5.2 Boundary Layers

In general, for a typical boundary layer, we must account for pressure gradient. Ignoring effects of normal Reynolds stresses and introducing the eddy viscosity to determine the Reynolds shear stress, the two-dimensional ($j = 0$) and axisymmetric ($j = 1$) boundary-layer equations are as follows.

$$\frac{\partial U}{\partial x} + \frac{1}{y^j}\frac{\partial}{\partial y}\left(y^j V\right) = 0 \tag{3.139}$$

$$\rho U\frac{\partial U}{\partial x} + \rho V\frac{\partial U}{\partial y} = -\frac{dP}{dx} + \frac{1}{y^j}\frac{\partial}{\partial y}\left[y^j(\mu + \mu_T)\frac{\partial U}{\partial y}\right] \tag{3.140}$$

The appropriate boundary conditions follow from the no slip condition at the surface and from insisting that $U \to U_e$ as we approach the boundary-layer edge. Consequently, we must solve Equations (3.139) and (3.140) subject to

$$\left.\begin{array}{rcl} U(x,0) &=& 0 \\ V(x,0) &=& 0 \\ U(x,y) &\to& U_e(x) \quad as \quad y \to \delta(x) \end{array}\right\} \tag{3.141}$$

where $\delta(x)$ is the boundary-layer thickness.

The Cebeci-Smith model has been applied to a wide range of boundary-layer flows and has enjoyed a great deal of success. Figure 3.13, for example, compares computed skin friction, c_f, and shape factor, H, for a constant-pressure (flat-plate) boundary layer with Coles' [Coles and Hirst (1969)] correlation of experimental data. Results are expressed as functions of Reynolds number based on momentum thickness, Re_θ. As shown, model predictions virtually duplicate correlated values.

The model remains reasonably accurate for favorable pressure gradient and for mild adverse pressure gradient. Because the model has been fine tuned for boundary-layer flows, differences between computed and measured velocity profiles generally are small. However, integral parameters such as momentum thickness and shape factor often show 10% differences from measured values.

Figure 3.14 compares computed and measured boundary layer properties for two of the flows considered in the 1968 AFOSR-IFP-Stanford

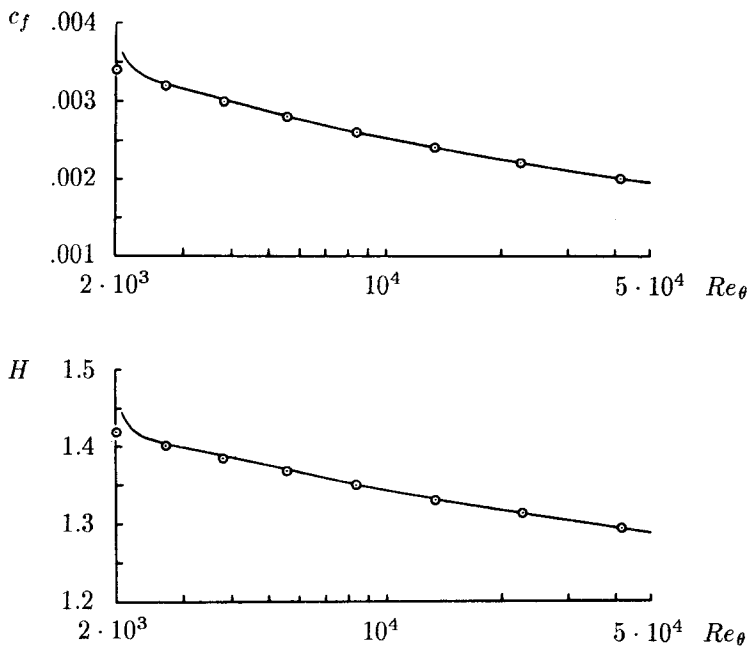

Figure 3.13: Comparison of computed and correlated shape factor and skin friction for flat-plate boundary layer flow; ⊙ Coles; —— Cebeci-Smith model. [From Kline et al. (1969) — Used with permission.]

Conference on the Computation of Turbulent Boundary Layers (this conference is often referred to colloquially as Stanford Olympics I). For both cases, computed and measured velocity profiles are nearly identical. Flow 3100 is two dimensional with a mild favorable pressure gradient. Despite the close agreement in velocity profiles overall, differences in shape factor are between 8% and 10%. Flow 3600 is axisymmetric with an adverse pressure gradient. For this flow, shape factors differ by less than 5%.

The Baldwin-Lomax model also closely reproduces correlated values of flat-plate boundary-layer properties. It performs reasonably well even for adverse pressure gradient as evidenced in Figure 3.15. The flow considered is an incompressible boundary layer in an increasingly adverse pressure gradient which has been studied experimentally by Samuel and Joubert [see Kline et al. (1981)]. The close agreement between theory and experiment for this flow is actually remarkable. This boundary layer was presumed to be a "simple" flow for the 1980-81 AFOSR-HTTM-Stanford Conference on Complex Turbulent Flows (known colloquially as Stanford Olympics II).

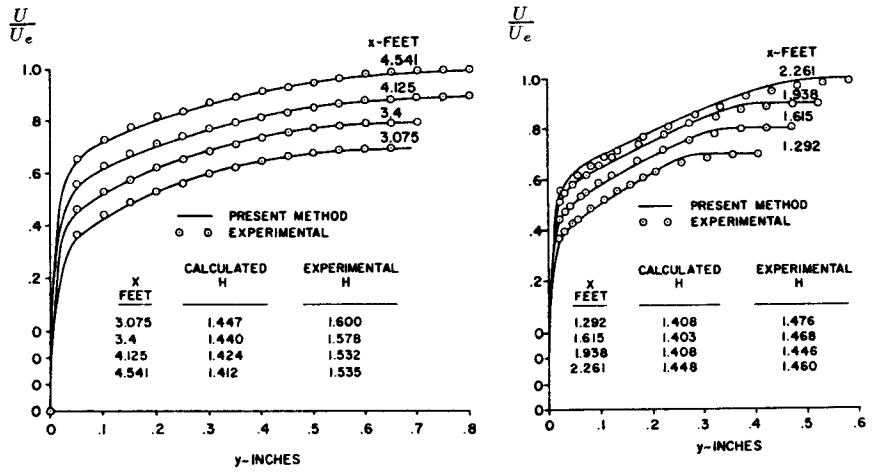

Flow 3100 Flow 3600

Figure 3.14: Comparison of computed and measured boundary layer velocity profiles and shape factor for flows with nonzero pressure gradient; Cebeci-Smith model. [From Kline et al. (1969) — Used with permission.]

However, as we will discuss further in Chapter 4, it proved to be the Achilles heel of the best turbulence models of the day.

Figure 3.16 compares computed and measured skin friction for Flow 3300 of the 1968 AFOSR-IFP-Stanford Conference on the Computation of Turbulent Boundary Layers. This flow, also known as Bradshaw Flow C, has a strongly adverse pressure gradient that is gradually relaxed and corresponds to an experiment performed by Bradshaw (1969). It was generally regarded as one of the most difficult to predict of all flows considered in the Conference. As shown, both models predict skin friction significantly higher than measured. The Cebeci-Smith value for c_f at the final station ($x = 7$ ft.) is 22% higher than the measured value. The Baldwin-Lomax value exceeds the measured value at $x = 7$ ft. by 36%.

3.6 Separated Flows

All of the applications in the preceding section are for attached boundary layers. We turn now to flows having an adverse pressure gradient of sufficient strength to cause the boundary layer to separate. Separation occurs

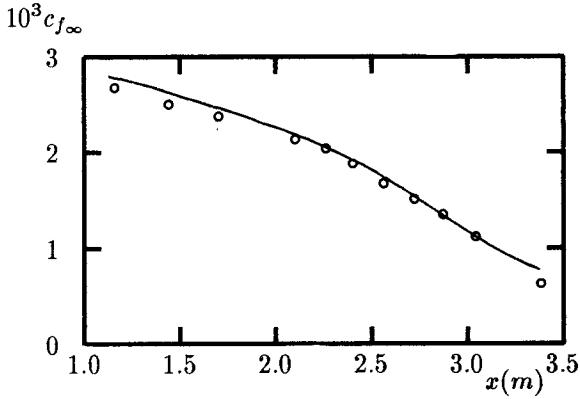

Figure 3.15: Computed and measured skin friction for Samuel-Joubert's adverse pressure gradient flow; —— Baldwin-Lomax model; o Samuel-Joubert.

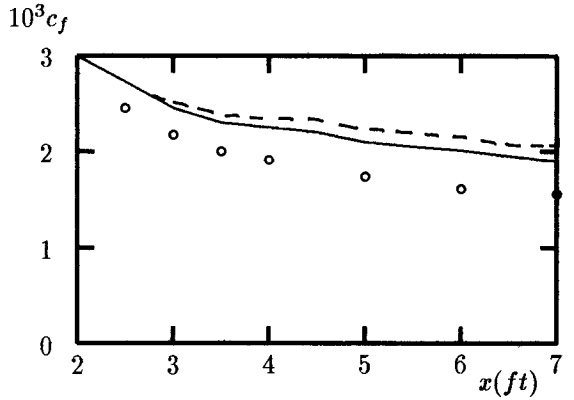

Figure 3.16: Comparison of computed and measured skin friction for Bradshaw Flow C; —— Cebeci-Smith; - - - Baldwin-Lomax; o Bradshaw.

in many practical applications including stalled airfoils, flow near the stern of a ship, flow through a diffuser, etc. Engineering design would be greatly enhanced if our turbulence model were a reliable analytical tool for predicting separation and its effect on surface pressure, skin friction and heat transfer. Unfortunately, algebraic models are quite unreliable for separated flows.

When a boundary layer separates, the streamlines are no longer nearly parallel to the surface as they are for attached boundary layers. We must solve the full Reynolds-averaged Navier-Stokes equation [Equation (2.24)], which includes all components of the Reynolds-stress tensor. In analogy to Stokes hypothesis for laminar flow, we set

$$\tau_{ij} = 2\mu_T S_{ij} \tag{3.142}$$

where S_{ij} is the mean strain-rate tensor defined by

$$S_{ij} = \frac{1}{2}[U_{i,j} + U_{j,i}] \tag{3.143}$$

Figure 3.17 is typical of separated flow results for an algebraic model. Menter (1992b) applied the Baldwin-Lomax model to an axisymmetric flow with a strong adverse pressure gradient. The experiment was conducted by Driver (1991). Inspection of the skin friction shows that the Baldwin-Lomax model yields a separation bubble nearly twice as long as the experimentally observed bubble. The corresponding rise in pressure over the separation region is 15% to 20% higher than measured. As pointed out by Menter, the Cebeci-Smith model yields similar results.

It is not surprising that a turbulence model devoid of any information about flow history will perform poorly for separated flows. On the one hand, the mean strain-rate tensor undergoes rapid changes in a separated flow associated with the curved streamlines over and within the separation bubble. On the other hand, the turbulence adjusts to changes in the flow on a time scale unrelated to the mean rate of strain. Rotta (1962), for example, concludes from analysis of experimental data that when a turbulent boundary layer is perturbed from its equilibrium state, a new equilibrium state is not attained for at least 10 boundary-layer thicknesses downstream of the perturbation. In other words, separated flows are very much out of "equilibrium." The Boussinesq approximation, along with all the "equilibrium" approximations implicit in an algebraic model, can hardly be expected to provide an accurate description for separated flows.

Attempts have been made to remedy the problem of poor separated flow predictions with the Cebeci-Smith model. Shang and Hankey (1975) introduced the notion of a relaxation length, L, to account for upstream

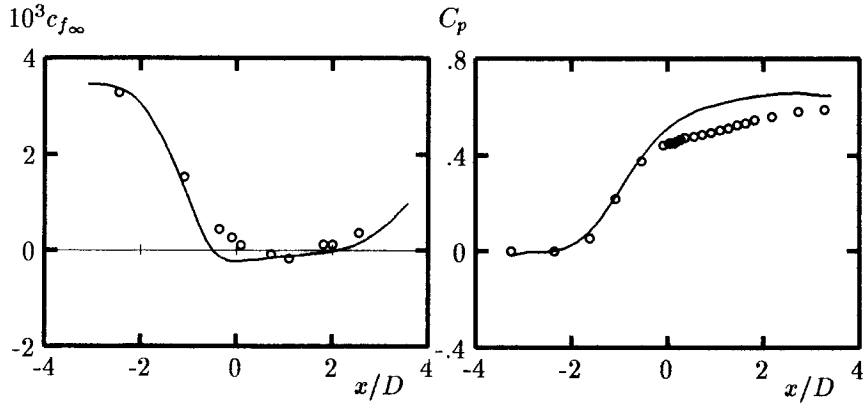

Figure 3.17: Computed and measured flow properties for Driver's separated flow; —— Baldwin-Lomax; o Driver.

turbulence history effects. They introduced what they called a **relaxation eddy viscosity model** and determined the eddy viscosity as follows.

$$\mu_T = \mu_{T_{eq}} - (\mu_{T_{eq}} - \mu_{T_1}) e^{-(x-x_1)/L} \tag{3.144}$$

The quantity $\mu_{T_{eq}}$ denotes the equilibrium eddy viscosity given by Equations (3.110) through (3.113), while μ_{T_1} is the value of the eddy viscosity at a reference point, $x = x_1$, upstream of the separation region. Typically, the relaxation length is about $5\delta_1$, where δ_1 is the boundary-layer thickness at $x = x_1$. The principal effect of Equation (3.144) is to reduce the Reynolds stress from the "equilibrium" value predicted by the Cebeci-Smith model. This mimics the experimental observation that the Reynolds stress remains nearly frozen at its initial value while it is being convected along streamlines in the separation region, and approaches a new equilibrium state exponentially.

In a similar vein, Hung (1976) proposed a differential form of Equation (3.144), viz.,

$$\frac{d\mu_T}{dx} = \frac{\mu_{T_{eq}} - \mu_T}{L} \tag{3.145}$$

Hung (1976) exercised these relaxation models in several supersonic shock-separated flows. He was able to force close agreement between computed and measured locations of the separation point and the surface pressure distribution. However, he found that these improvements came at the expense of increased discrepancies between computed and measured skin friction, heat transfer and reattachment-point location.

3.7 The 1/2-Equation Model

Johnson and King (1985) [see also Johnson (1987) and Johnson and Coakley (1990)] have devised a "non-equilibrium" version of the algebraic model. Their starting point is a so-called "equilibrium" algebraic model in which the eddy viscosity is

$$\mu_T = \mu_{T_o} \tanh(\mu_{T_i}/\mu_{T_o}) \tag{3.146}$$

Inner Layer:

The inner layer viscosity, μ_{T_i}, is similar to the form used in the Cebeci-Smith and Baldwin-Lomax models. However, the dependence on velocity gradient has been replaced by explicit dependence on distance from the surface, y, and two primary velocity scales, u_τ and u_m, as follows:

$$\mu_{T_i} = \rho \left[1 - \exp\left(-\frac{u_D y/\nu}{A^+}\right)\right]^2 \kappa u_s y \tag{3.147}$$

$$u_s = \sqrt{\rho_w/\rho}\, u_\tau(1-\gamma_2) + \sqrt{\rho_m/\rho}\, u_m \gamma_2 \tag{3.148}$$

$$\gamma_2 = \tanh(y/L_c) \tag{3.149}$$

$$L_c = \frac{\sqrt{\rho_w}\, u_\tau}{\sqrt{\rho_w}\, u_\tau + \sqrt{\rho_m}\, u_m} L_m \tag{3.150}$$

$$L_m = \begin{cases} \kappa y_m, & y_m/\delta \le C_1/\kappa \\ C_1\delta, & y_m/\delta > C_1/\kappa \end{cases} \tag{3.151}$$

$$u_m = \sqrt{\tau_m/\rho_m} \tag{3.152}$$

$$u_D = \max[u_m, u_\tau] \tag{3.153}$$

where subscript m denotes the value at the point, $y = y_m$, at which the Reynolds shear stress, τ_{xy}, assumes its maximum value denoted by $\tau_m = (\tau_{xy})_{max}$. Additionally u_τ is the conventional friction velocity and ρ_w is the density at the surface, $y = 0$. In its original form, this model used only the velocity scale u_m in Equation (3.147). This scale proved to provide better predictions of velocity profile shape for separated flows than the velocity-gradient prescription of Prandtl [Equation (3.15)]. Later, the secondary velocity scales u_s and u_D were added to improve predictions for reattaching flows and for flows with nontrivial effects of compressibility.

Outer Layer:

The "non-equilibrium" feature of the model comes in through the appearance of a "nonequilibrium parameter," $\sigma(x)$, so that:

$$\mu_{T_o} = \alpha \rho U_e \delta_v^* F_{Kleb}(y;\delta)\sigma(x) \tag{3.154}$$

Comparison of this equation with Equation (3.113) shows that the outer layer viscosity, μ_{T_o}, is equal to the prescription used in the Cebeci-Smith model multiplied by $\sigma(x)$. The Johnson-King model solves the following **ordinary differential equation** for the maximum value of the Reynolds shear stress:

$$U_m \frac{d}{dx}\left(\frac{\tau_m}{\rho_m}\right) = a_1 \frac{[(u_m)_{eq} - u_m]}{L_m}\left(\frac{\tau_m}{\rho_m}\right) - C_{dif}\frac{(\tau_m/\rho_m)^{3/2}}{[C_2\delta - y_m]}|1 - \sigma^{1/2}(x)| \tag{3.155}$$

where $(u_m)_{eq}$ is the value of u_m according to the "equilibrium" algebraic model [$\sigma(x) = 1$]. The first term on the right-hand side of Equation (3.155) is reminiscent of Hung's relaxation model [Equation (3.145)]. The second term is an estimate of the effect of turbulent diffusion on the Reynolds shear stress. Equation (3.155) is solved along with the Reynolds-averaged equations to determine τ_m. As the solution proceeds, the coefficient $\sigma(x)$ is determined so that the maximum Reynolds shear stress is given by

$$\tau_m = (\mu_T)_m \left(\frac{\partial U}{\partial y} + \frac{\partial V}{\partial x}\right)_m \tag{3.156}$$

That is, the μ_T distribution is adjusted to agree with τ_m. In using this model, computations must be done iteratively since $\sigma(x)$ is unknown a priori, wherefore the value from a previous iteration or an extrapolated value must be used in solving Equation (3.155) for τ_m.

Closure Coefficients:

$$\left.\begin{array}{lll} \kappa = 0.40, & \alpha = 0.0168, & A^+ = 17 \\ a_1 = 0.25, & C_1 = 0.09, & C_2 = 0.70 \\ C_{dif} = 0.50 & \text{for } \sigma(x) \geq 1; & 0 \text{ otherwise} \end{array}\right\} \tag{3.157}$$

The general idea of this model is that the Reynolds shear stress adjusts to departures from "equilibrium" at a rate different from that predicted by the algebraic model. The ordinary differential equation for τ_m is used to account for the difference in rates. Because this equation is an **ordinary**, as opposed to a **partial**, differential equation, the turbulence community has chosen the curious terminology **1/2-Equation Model** to describe this model. It is unclear whether this means it has half the number of dimensions (but then, it would have to be a 1/3-Equation Model for three-dimensional applications) or if partial differential equations are twice as hard to solve as ordinary differential equations.

Menter (1992b) has applied the Johnson-King model to the attached boundary-layer flow of Samuel and Joubert [see Kline et al. (1981)] and

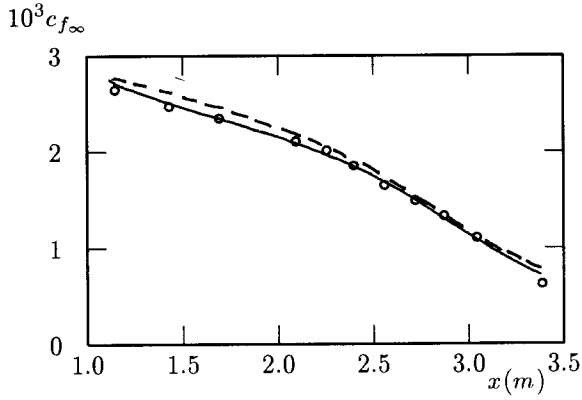

Figure 3.18: Computed and measured skin friction for Samuel-Joubert's adverse pressure gradient flow; —— Johnson-King; - - - Baldwin-Lomax; o Samuel-Joubert.

to Driver's (1991) separated flow. Figures 3.18 and 3.19 compare computed and measured values; results for the Baldwin-Lomax model are also included. As shown, the Johnson-King model predictions are somewhat closer to measured values for the Samuel-Joubert flow. For the separated case, Johnson-King predictions are much closer to measurements, most notably in the size of the separation region.

3.8 Range of Applicability

Algebraic models are the simplest and easiest to implement of all turbulence models. They are conceptually very simple and rarely cause unexpected numerical difficulties. Because algebraic models are so easy to use, they should be replaced only where demonstrably superior alternatives are available.

The user must always be aware of the issue of **incompleteness**. These models will work well only for the flows for which they have been fine tuned. There is very little hope of extrapolating beyond the established data base for which an algebraic model is calibrated. We need only recall that for the four free shear flows considered in Section 3.3, four different values for the mixing length are needed—and none of these lengths is appropriate for wall-bounded flows!

On balance, both the Cebeci-Smith and Baldwin-Lomax models faithfully reproduce skin friction and velocity profiles for incompressible turbulent boundary layers provided the pressure gradient is not too strong.

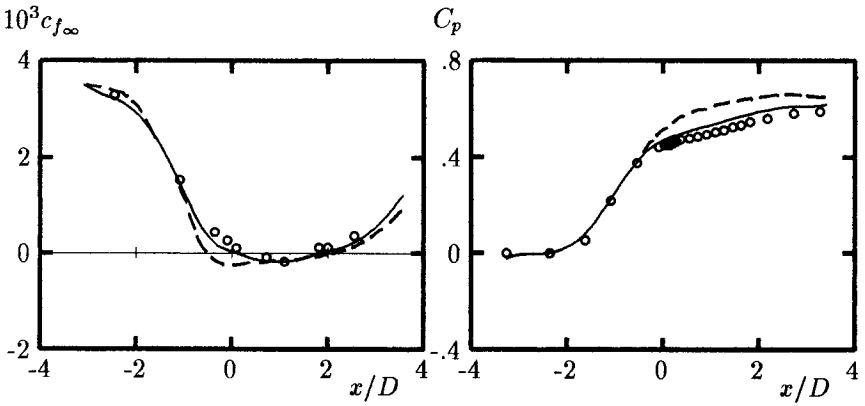

Figure 3.19: Computed and measured flow properties for Driver's separated flow; —— Johnson-King; - - - Baldwin-Lomax; o Driver.

Neither model is clearly superior to the other: the accuracy level is about the same for both models. The chief virtue of the Baldwin-Lomax model over the Cebeci-Smith model is its independence from properties such as δ_v^* that can be difficult to compute accurately in complex flows. Its other differences from the Cebeci-Smith model are probably accidental. However, neither model is reliable for separated flows. Despite this well-known limitation, many incautious researchers have applied these models to extraordinarily complex flows where their only virtue is that they don't cause the computations to blow up.

The Johnson-King model offers a promising modification that removes much of the inadequacy of algebraic models for separated flows. However, like algebraic models, the Johnson-King model provides no information about the turbulence length scale and is thus **incomplete**. Consequently, it shares many of the shortcomings of the underlying algebraic model. **On the negative side**, the improved agreement between theory and experiment has been gained at the expense of the elegance and simplicity of the Cebeci-Smith model. The number of ad hoc closure coefficients has increased from three to seven, and the model inherently requires an iterative solution procedure. The model is also formulated specifically for wall-bounded flows and is thus restricted to such flows, i.e., the model is highly geometry dependent. **On the positive side**, the Johnson-King model has been applied to many transonic flows that tend to be particularly difficult to predict with modern turbulence models. The model's track record has been quite good with such flows. On balance, this model appears to be a useful engineering design tool, within its verified range of applicability.

Problems

3.1 For the far wake, verify that the solution to Equations (3.45) is given by Equations (3.46) - (3.48).

3.2 For the mixing layer, beginning with Equation (3.65), introduce Equations (3.68) - (3.71) and derive Equation (3.73).

3.3 For the jet, begin with Equation (3.83) and derive Equation (3.86).

3.4 Using Equation (3.25) to represent the eddy viscosity, generate a similarity solution for the far wake. Obtain the exact closed-form solution, and determine the value of χ by forcing agreement with the corresponding $u_o(x)$ and $\delta(x)$ derived in this chapter. The following integral will be useful when you apply the integral constraint.

$$\int_0^\infty e^{-\xi^2} d\xi = \frac{\sqrt{\pi}}{2}$$

3.5 Using Equation (3.25) to represent the eddy viscosity, generate a similarity solution for the plane jet. Obtain the exact closed-form solution, and determine the value of χ by forcing agreement with the corresponding $u_o(x)$ and $\delta(x)$ derived in this chapter. The following integrals will be useful in deriving the solution.

$$\int \frac{dx}{c^2 - x^2} = \frac{1}{c} \tanh^{-1}\left(\frac{x}{c}\right) + \text{constant}$$

$$\int_0^\infty \left[1 - \tanh^2 \xi\right]^2 d\xi = \frac{2}{3}$$

3.6 Show that using Equation (3.98) for the mixing length in the viscous sublayer yields a velocity that behaves according to:

$$U^+ \approx y^+ - \frac{\kappa^2}{3}(y^+)^3 + \cdots \quad \text{as} \quad y^+ \to 0$$

3.7 Using a standard numerical integration scheme such as the Runge-Kutta method, determine the constant, B, in the law of the wall implied by the mixing-length model. That is, solve the following equation for U^+.

$$(1 + \mu_T^+)\frac{dU^+}{dy^+} = 1$$

Integrate from $y^+ = 0$ to $y^+ = 500$ and calculate the limiting value of B as $y^+ \to \infty$ from examination of

$$B = U^+ - \frac{1}{\kappa}\ell n y^+ \quad \text{at} \quad y^+ = 200, 300, 400 \text{ and } 500$$

Do the computation with the mixing length given by:

(a) Equation (3.98)

(b) Equation (3.105)

NOTE: To avoid truncation error, verify the following limiting form of the equation for dU^+/dy^+.

$$\frac{dU^+}{dy^+} \approx 1 - \left(\ell^+_{mix}\right)^2 + 2\left(\ell^+_{mix}\right)^4 + \cdots \quad \text{as} \quad \ell^+_{mix} \to 0$$

Use this asymptotic form very close to $y^+ = 0$.

3.8 For a constant-pressure turbulent boundary layer, the skin friction and displacement thickness are approximately

$$c_f \approx 0.045 Re_\delta^{-1/4} \quad \text{and} \quad \delta^* \approx \frac{1}{8}\delta$$

where $Re_\delta = U_e\delta/\nu$ is Reynolds number based on δ. Note also that, by definition, $c_f = 2u_\tau^2/U_e^2$. Assuming the matching point always occurs in the log layer so that $\partial U/\partial y = u_\tau/(\kappa y)$, make a graph of y_m/δ and y_m^+ versus Re_δ for the Cebeci-Smith model. Let Re_δ vary between 10^4 and 10^6. You should first rewrite the equations for μ_{T_i} and μ_{T_o} in terms of y/δ and Re_δ. Then, solve the resulting equation for y_m/δ with an iterative procedure such as Newton's method. Compare your numerical results with Equation (3.118).

3.9 Assume the velocity in a boundary layer for $y^+ \gg 1$ is given by

$$U^+ \approx \frac{1}{\kappa}\ell n y^+ + 5.0 + \frac{1}{\kappa}\sin^2\left(\frac{\pi y}{2\delta}\right)$$

Also, assume that $y_{max} \gg 26\nu/u_\tau$ for the Baldwin-Lomax model. Compute the quantities $y_{max}F_{max}$ and $C_{wk}y_{max}U^2_{dif}/F_{max}$ for this boundary layer. Then, noting that $c_f = 2u_\tau^2/U_e^2$, determine the largest value of c_f for which $F_{wake} = y_{max}F_{max}$.

3.10 For a turbulent boundary layer with surface mass transfer, the momentum equation in the sublayer and log layer simplifies to:

$$v_w \frac{dU}{dy} = \frac{d}{dy}\left[(\nu + \nu_T)\frac{dU}{dy}\right]$$

where v_w is the (constant) vertical velocity at the surface.

(a) Integrate once using the appropriate surface boundary conditions. Introduce the friction velocity, u_τ, in stating your integrated equation.

(b) Focusing now upon the log layer where $\nu_T \gg \nu$, what is the approximate form of the equation derived in Part (a) if we use the Cebeci-Smith model?

(c) Verify that the solution to the simplified equation of Part (b) is

$$2\frac{u_\tau}{v_w}\sqrt{1 + v_w U/u_\tau^2} = \frac{1}{\kappa}\ell n y + \text{constant}$$

3.11 Generate a solution for channel and pipe flow using a mixing-length model with the mixing length in the inner and outer layers given by

$$\ell_{mix} = \begin{cases} \kappa y\left[1 - e^{-y^+/26}\right] & , \text{ Inner Layer} \\ .09R & , \text{ Outer Layer} \end{cases}$$

where R is channel half-height or pipe radius. Use a numerical integration scheme such as the Runge-Kutta method, or modify Program PIPE (Appendix C). Compare computed skin friction with Equations (3.137) and (3.138). **See NOTE below.**

3.12 Generate a solution for pipe flow using a mixing-length model with the mixing length given by Nikuradse's formula, i.e.,

$$\ell_{mix}/R = 0.14 - 0.08(1 - y/R)^2 - 0.06(1 - y/R)^4$$

where R is pipe radius. Use a numerical integration scheme such as the Runge-Kutta method, or modify Program PIPE (Appendix C). Compare computed skin friction with Equation (3.138). **See NOTE below.**

NOTE: To assist in presenting your results, verify that $c_f = 2/(U^+_{avg})^2$ and $Re_D = 2U^+_{avg}R^+$ where $R^+ = u_\tau R/\nu$ and U_{avg} is the average velocity

across the channel/pipe. Also, to avoid truncation error, verify the following limiting form of the equation for dU^+/dy^+ in the limit $\ell^+_{mix} \to 0$.

$$\frac{dU^+}{dy^+} \approx \left(1 - \frac{y^+}{R^+}\right)\left[1 - \left(1 - \frac{y^+}{R^+}\right)(\ell^+_{mix})^2 + 2\left(1 - \frac{y^+}{R^+}\right)^2 (\ell^+_{mix})^4\right]$$

Use this asymptotic form very close to $y^+ = 0$.